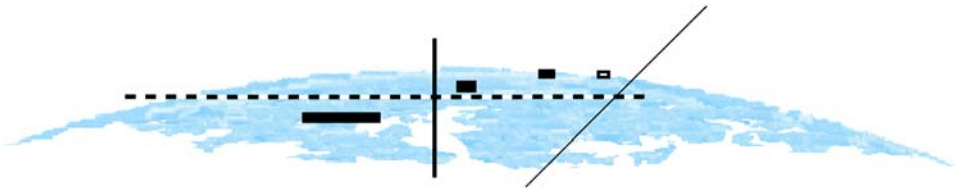

GeoForschungsZentrum Potsdam

STIFTUNG DES ÖFFENTLICHEN RECHTS

Scientific Technical Report

ISSN 1610-0956

Ingo Sasgen, Detlef Wolf, Zdeněk Martinec,
Volker Klemann, Jan Hagedoorn

Geodetic signatures of glacial changes in Antarctica: rates of geoid-height change and radial displacement due to present and past ice-mass variations

Scientific Technical Report STR05/01

DOI: 10.2312/GFZ.b103-05011

DOI: 10.2312/GFZ.b103-05011

Contents

DOI: 10.2312/GFZ.b103-05011

DOI: 10.2312/GFZ.b103-05011

Summary

This study is concerned with the forward modelling of the present-day glacial-isostatic adjustment (GIA) of the earth to present and past changes of the Antarctic ice sheet (AIS). We predict temporal variations in the geoid height and topographic height within the context of the Gravity Recovery and Climate Experiment (GRACE) satellite mission and terrestrial Global Positioning System (GPS) stations in Antarctica.

We first adopt an elastic-compressible earth model and calculate the earth's response to seasonal (< 1 a) and secular (~ 100 a) ice-mass changes. Then, we consider a viscoelastic-incompressible earth model and determine the earth's response to the melting of the AIS since the last glacial maximum (LGM), i.e. the post-glacial rebound (PGR). Both models are radially symmetric and self gravitating. A range of viscosity values account for the uncertainty in the viscosity stratification and the lateral heterogeneity of the mantle beneath Antarctica. We employ six load models simulating the most important temporal aspects of the AIS's evolution. Finally, we predict the geoid-height change and the land uplift and compare them with recent GRACE observations and determinations of the uplift rate for the permanent GPS stations along the Antarctic coast.

In the spatial domain, the secular rate of geoid-height change exhibits a strong negative value of -3.7 mm/a along the coast of West Antarctica. This corresponds to the glaciers in this region losing significant mass. Moreover, PGR-induced positive values of up to 1.5 mm/a are found over the present major ice shelves. The seasonal variation of the geoid height is largest over the coastal regions, where its double amplitude is 10 mm.

In the spectral domain, the secular geoid-height change is dominated at low degrees by the PGR-induced changes. With increasing degree, the secular ice-mass balance gains importance. The seasonal signal is about one order of magnitude higher. The predictions remain well above the estimated GRACE accuracy ($\sim 10^{-3}$ mm/a) even for higher degrees (~ 30).

The largest land-uplift rates are due to PGR and occur over the present major ice shelves. The values predicted strongly depend on the mantle viscosity adopted and lie between 4 and 25 mm/a. The values for the secular ice-mass changes are insignificant. The uplift rates at the GPS stations considered (~ 4 mm/a) do not reflect the bulk features of the ice retreat and, therefore, do not provide useful constraints on the AIS's evolution since the LGM. For this purpose, the determination of land-uplift rates near the Amery, Larsen and Ronne Ice Shelves is of importance.

DOI: 10.2312/GFZ.b103-05011

Zusammenfassung

Diese Arbeit beschäftigt sich mit der Vorwärtsmodellierung der gegenwärtigen glazialisostatischen Ausgleichsbewegung (GIA) der Erde aufgrund heutiger und vergangener Änderungen des Antarktischen Eisschildes (AIS). Im Zusammenhang mit der Gravity Recovery and Climate Experiment (GRACE) Satellitenmission und terrestrischen Global Positioning System (GPS) Stationen in der Antarktis werden Vorhersagen über die GIA-induzierte zeitliche Schwankung der Geoidhöhe und der topographischen Höhe getroffen.

Zunächst verwenden wir ein elastisch-kompressibles Erdmodell und berechnen die Antwort der Erde auf saisonale ($< 1\,\mathrm{a}$) und säkulare ($\sim 100\,\mathrm{a}$) Eismassenänderungen. Danach betrachten wir ein viskoelastisch-inkompressibles Erdmodell und bestimmen die Antwort der Erde auf das Abschmelzen des AIS seit dem Letzten Glazialen Maximum (LGM), d.h. den Post-Glacial Rebound (PGR). Beide Modelle sind radialsymmetrisch und selbstgravitierend. Eine Spanne von Viskositätswerten berücksichtigt die Unsicherheit der Viskositätsschichtung und die laterale Heterogenität des Mantels unter der Antarktis. Wir verwenden sechs Lastmodelle, welche die wichtigsten zeitlichen Aspekte der Entwicklung des AIS simulieren. Schließlich prädizieren wir die Geoidhöhenänderung und Landhebung und vergleichen diese mit neuesten GRACE-Beobachtungen und Bestimmungen der Hebungsrate für die permanenten GPS-Stationen entlang der Antarktischen Küste.

Im Raumbereich zeigt die säkulare Rate der Geoidhöhenänderung einen negativen Wert von $-3.7\,\mathrm{mm/a}$ entlang der Küste der Westantarktis. Dies entspricht bedeutenden Massenverlusten der Gletscher in dieser Gegend. Desweiteren finden sich PGR-induzierte positive Werte von bis zu $1.5\,\mathrm{mm/a}$ über den heutigen großen Schelfeisgebieten. Die saisonale Schwankung der Geoidhöhe ist am größten über den Küstengebieten, wo ihre Doppelamplitude $10\,\mathrm{mm}$ beträgt.

Im Spektralbereich wird die säkulare Geoidhöhenänderung bei niedrige Graden durch die PGR-induzierten Änderungen dominiert. Mit zunehmendem Grad gewinnt die säkulare Eismassenbilanz an Bedeutung. Das saisonale Signal liegt etwa eine Größenordung höher. Die Vorhersagen bleiben auch für höhere Grade (~ 30) deutlich über der geschätzten GRACE-Genauigkeit ($\sim 10^{-3}\,\mathrm{mm/a}$).

Die höchsten Landhebungsraten werden durch PGR verursacht und treten in den heutigen großen Schelfeisgebieten auf. Die vorhergesagten Werte hängen stark von der verwendeten Mantelviskosität ab und liegen zwischen 4 und $25\,\mathrm{mm/a}$. Die Werte für die säkularen Eismassenänderungen sind unbedeutend. Die Landhebungsraten an den berücksichtigten GPS-Stationen ($\sim 4\,\mathrm{mm/a}$) geben nicht die wesentlichen Merkmale des Eisrückzugs wieder und eignen sich darum nicht als Randbedingung für die Entwicklung des AIS seit dem LGM. Zu diesem Zweck ist die Bestimmung von Landhebungsraten nahe der Amery-, Larsen- und Ronne-Eisschelfe von Bedeutung.

DOI: 10.2312/GFZ.b103-05011

1

Introduction

The Antarctic ice sheet (AIS) is the largest contingent ice mass on earth and, since its initial formation ~ 30 Ma ago, its development has been closely linked to global climate and sea-level changes. The improved knowledge of its current state and development in the near future will contribute to the reliability of climate models, which provide estimates of potential global temperature and sea-level changes for the centuries to come.

One promising method of determining the changes of the AIS is offered by the recently launched Gravity Recovery and Climate Experiment (GRACE) satellite mission, which monitors the temporal variations of the earth's gravity field due to mass changes within and on the the earth. For Antarctica, two sources of mass changes provide the main contributions to the GRACE signal: (a) present glacial changes of the ice sheet and (b) mass changes within the earth related to the ongoing viscoelastic relaxation of the earth in response to the retreat of the larger ice masses present at the last glacial maximum (LGM). Besides perturbing the earth's gravity field, present and past ice-mass changes produce displacement of the earth's surface, which can be detected by an increasing number of terrestrial Global Positioning System (GPS) receivers installed on the Antarctic continent.

So far, knowledge about present and past glacial changes in Antarctica has been limited. In this context, the present forward-modelling study provides predictions for future GRACE and GPS observations based on a range of plausible scenarios and time scales of changes of the AIS.

1.1 Glacial-isostatic adjustment

The body of the earth responds to glacial changes and associated sea-level variations with deformation, seeking to obtain a new equilibrium state. This process is called glacial-isostatic adjustment (GIA). The present study focusses on the AIS and considers two aspects of GIA: the elastic response to present ice-mass changes and the viscoelastic response to past ice-mass changes also referred to as post-glacial rebound (PGR).

The most important redistribution of ice mass is associated with the glacial cycles. Paleoclimatic records indicate that over the last 1 Ma, glacial and interglacial epochs alternated with a period of ~ 100 ka. This period coincides with the variation of the earth's orbital eccentricity, the Milankovich cycle of 95.8 ka, and several theories about its influence on the glacial cycles have been proposed (e.g. Roe & Allen, 1999). The glaciation phase, marked by a steady growth of ice, generally spans ~ 90 ka and is followed by a rapid deglaciation phase that lasts only ~ 10 ka. There is ample

DOI: 10.2312/GFZ.b103-05011

evidence that the LGM occurred ~ 21 ka before present (BP). Since then, global ice masses have decreased to approximately one third of the LGM value, causing a global mean sea-level rise of ~ 110 m ESL[1]. The ongoing adjustment of the earth's body to the redistribution of ice and water masses is evident in various phenomena, which have been studied not only to infer the extent and amount of the former ice masses, but also to obtain constraints on the earth's viscosity.

GIA causes temporal changes of the earth's gravitational field, described as deformation of the surface of equal gravitational potential, the geoid. The state of isostatic disequilibrium in regions with past ice-mass loss results in a negative geoid height; the process of PGR, meaning an influx of mantle material, reduces the the geoid low. A well-known example is found in north-eastern Canada, where a geoid height of -40 m indicates that the earth has not fully regained isostatic equilibrium after the retreat of the Laurentide ice sheet. However, in this region, at least half of the geoid depression is attributed to a density anomaly driving mantle convection (e.g. Mitrovica & Vermeersen, 2001). The geoid-height changes associated with present-day glacial changes are dominated by the direct attraction of the ice and water masses involved. Changes due to the earth's elastic response are comparatively small.

GIA is also evident in the displacement of the earth's surface. A well-studied example is the land uplift occurring in the Gulf of Bothnia, Fennoscandia, an area which was depressed by an ice sheet of 2 to 3 km thickness at the LGM. The ongoing adjustment following the ice sheet's retreat has been monitored by GPS studies, such as the Baseline Inferences for Fennoscandian Rebound Observations, Sea Level and Tectonics (BIFROST) project (Davis & members of BIFROST, 1996; Scherneck *et al.*, 2003). The results determine the vertical and horizontal surface displacements, indicating land-uplift rates of up to 8 mm/a close to the former load centre.

Another well-known effect of GIA is its influence on the relative sea level (RSL), measured at tide-gauge stations distributed over the globe. In general, the retreat of a continent-based ice sheet causes land uplift, whereas the water discharged into the ocean causes subsidence of the ocean floor. The associated redistribution of mass within and on the earth changes the geoid height, which, by definition, is identical to the mean sea-level height. RSL observations indicate the sea-level height in reference to a point on land. Provided there is no ESL change, the RSL change is therefore a measure of the difference between the geoid-height change and the surface displacement and contains information on GIA.

GIA also causes variations of the position of the earth's rotation axis with respect to an earth-fixed system: the true polar wander (TPW) and the duration of a single rotation: the length of day (LOD). Mass redistributions within and on the earth change the inertia tensor of the earth, which is visible as TPW. The LOD is proportional to the moment of inertia about the earth's spin axis, which, in turn, is proportional to the zonal harmonic of degree two of the earth's geopotential. At present, this results in an acceleration of the earth's rotation, i.e. a shortening of the LOD (e.g. Nakada & Okuno, 2003). However, GIA-induced variations of the earth's rotation parameters are masked by other processes, e.g. the convective flow in the mantle, the direct effect of the present redistribution of ice and water masses and changes in the pressure fields at the core-mantle boundary (e.g. Mitrovica & Vermeersen, 2001).

[1]Equivalent sea level (ESL) is a volume measure and here defined as the water volume equivalent to the ice mass under consideration divided by the global ocean area, fixed to 362×10^6 km^2.

DOI: 10.2312/GFZ.b103-05011

1.2 Antarctic ice sheet

The grounded portion of the AIS covers 95 % of the continent and has an area of $\sim 12 \times 10^6$ km^2. Its current mass is estimated at 28×10^6 Gt or 61 m ESL, which is about ten times that of the Greenland Ice Sheet (Huybrechts, 2002). The Transantarctic Mountains divide Antarctica into West and East Antarctica. The western part of the AIS is marine based and interacts with the global ocean currents. This has made it unstable and sensitive to global climate changes during the Quaternary. In contrast to this, most of the eastern part of the AIS continues to rest on bedrock above sea level and is therefore considered to be more stable (Hambrey & Hubbard, 2004 *[online]*).

Along the Antarctic Peninsula, mountain glaciers are prevalent, which differ from the rest of the AIS by extensive surface melting in the summer and by their influence on the regional climate. Their location at relatively low latitudes and exposition to the ocean make them likely to be sensitive indicators of global climate changes, even if they are not representative of the rest of the AIS. Rock outcrops primarily occur along the Transantarctic Mountains and the coastal fringe, their area amounting to only 0.4 % of the continent.

Contemporary annual snow accumulation over the grounded portion of the AIS is estimated at 1811 Gt or −4.9 mm ESL (Vaughan *et al.*, 1999). Most of the snow is locked into the ice sheet and discharged by outlet glaciers, which feed the ice shelves in the periphery of the continent. From the ice shelves, ice is mainly lost by iceberg calving and basal melting. Any imbalance between annual accumulation and discharge leads to an interannual ice-mass change, which contributes to the present global mean sea-level rise estimated at 1.8 mm/a (Church, 2002).

The long-term changes (10 to 100 a) of the AIS, in the following referred to as secular ice-mass changes, have recently been also investigated. The global mean sea-level contribution of the portion of the AIS studied (58 %) has been estimated at (0.07 ± 0.07) mm/a ESL (Rignot & Thomas, 2002). This study also reveals that West Antarctica loses ice mass at a rate of (-45 ± 13) Gt/a, whereas East Antarctica gains ice mass at a rate of (19 ± 21) Gt/a.

At the LGM, the AIS extended approximately to the continental margin (Figure 1.1) and additional grounded ice mainly existed in the regions that are now the major ice shelves: the Amery, Ross, Larsen and Ronne Ice Shelves. An increasing amount of evidence indicates that the AIS contained $\sim(-12 \pm 6)$ m ESL additional ice at the LGM relative to that at present and that the main deglaciation initiated ~ 15 ka BP (e.g. Bentley, 1999; Anderson *et al.*, 2002). The exact distribution of ice at the LGM, the details of its disintegration and the impact of the sea-level rise associated with the retreat of the northern-hemisphere ice sheets are still under debate.

1.3 Satellite-based geodetic observations

Far less is known about the AIS than about the Greenland ice sheet, which is mainly due to the size and inaccessibility of the former. For this reason, satellite-based geodetic observations present a promising alternative to ground-based methods.

One of the primary objectives of the GRACE satellite mission is to monitor the temporal variations of the geoid. It is expected that the accuracy of GRACE will be several orders of magnitudes higher than that of existing satellite measurements and

DOI: 10.2312/GFZ.b103-05011

Table 1.1: IGS stations in Antarctica. The GPS receivers are located on bedrock close to permanently occupied research stations and have been operational for at least 4 a. Locations are indicated in Figure 1.1.

ID	Station	Longitude (°E)	Latitude (°S)	Begin of observations
SYOG	Syowa	39.58	69.01	1999
MAW1	Mawson	62.87	67.60	1999
DAV1	Davis	77.97	68.58	1995
CAS1	Casey	110.52	66.28	1995
MCM4	Mc Murdo	166.67	77.84	1995
OHIG	O'Higgins	302.10	63.32	1995
VESL	Sanae IV	357.16	71.67	1999

be $\sim 10^{-3}$ mm/a at a spatial resolution of a few hundred km (Wahr & Velicogna, 2003). The mission has been in progress since November 2002 and will most likely exceed the scheduled lifetime of 5 a, thus further improving the accuracy. Latest GRACE solutions have determined the rate of geoid-height change with an accuracy at the 0.1 mm/a level and a spatial resolution of 1500 km.

Another promising satellite-based geodetic project is NASA's Ice, Cloud, and land Elevation Satellite (ICESat) for the determination of surface-elevation changes. The satellite is operative since January 2003 (NASA, 2004 *[online]*). For Antarctica, it will extend the data coverage to regions south of 81.5 °S, increase the accuracy of measurements along the ice margin and, hence, allow an improved assessment of the ice-thickness change.

GPS is now established as a standard technique to monitor the surface displacement. Its accuracy increases with the length of the interval of continuous measurements at the station considered. For a period of 5 a, measurement errors associated with uplift rates typically lie on the order of 1 mm/a. For Antarctica, the longest continuous measurements, ranging from 4 to 8 a, exist for 7 GPS stations operated by the International GPS Service for Geodynamics (IGS) (Table 1.1). As indicated in Figure 1.1, all 7 GPS receivers are located near the Antarctic coast, where rock outcrops exist.

At present, GPS stations are being installed along a transect of 800 km in the Prince Charles Mountains, East Antarctica (transect A–A′ in Figure 1.1), particularly for the purpose of detecting PGR-induced uplift. Reliable rates are expected within the next few years (Tregoning *et al.*, 2003).

Rock outcrops in the Transantarctic Mountains and along the Antarctic Peninsula would, in principle, allow a 3000 km GPS transect, stretching roughly from O'Higgins Station, West Antarctica, to Mc Murdo Station, East Antarctica (transect B–B′ in Figure 1.1). An assessment of the usefulness of such a GPS transect for detecting PGR is part of this study.

In the near future, the combination of GRACE, ICESat and GPS data will allow the separation of elevation changes induced by GIA from those induced by ice-mass imbalances and, thus, impose tighter constraints on the present mass balance and the history of the AIS (e.g. Wahr *et al.*, 2000; Velicogna & Wahr, 2002).

DOI: 10.2312/GFZ.b103-05011

1.4 Previous work

The vertical surface displacements associated with the glacial changes of the AIS have been predicted by several investigators (e.g. James & Ivins, 1995, 1997, 1998; Zwartz *et al.*, 1999). Thus, James & Ivins (1998) subjected a viscoelastic earth model to four distinct scenarios of secular ice-mass change, S1, S2 by mass, S2 by area and J92 (James & Ivins, 1997) and four, partially modified, Pleistocene deglaciation histories, LC79 (Lingle & Clark, 1979), ICE-3G (Tushingham & Peltier, 1991), ICE-4G (Peltier, 1994) and D91 (Denton *et al.*, 1991). The authors found that predicted uplift rates typically lie below 5 mm/a for contemporary ice-mass changes, with peak values of ~ 10 mm/a. The PGR-induced uplift rates are generally above 5 mm/a for most of West Antarctica, with peak values of ~ 16 mm/a.

Recently, with regard to the GRACE mission, GIA studies have specifically addressed the temporal variation of the geoid height (e.g. Kaufmann, 2000; Ivins *et al.*, 2001; Kaufmann, 2002). Thus, Kaufmann (2002) calculated present-day rates of geoid-height change for three Pleistocene glaciation histories, HUY (Huybrechts, 1990), ANT3 (Nakada & Lambeck, 1988) and ICE-3G (Tushingham & Peltier, 1991) in combination with three of the secular ice-mass balances mentioned above, S1, S2 by mass and J92. The author found that the PGR-induced rate of geoid-height change amounts to ~ 1 mm/a over West Antarctica and is significantly lower over East Antarctica. The present ice-mass changes influence the geoid on a smaller spatial scale, with amplitudes locally exceeding 3 to 4 mm/a.

Similar studies have predicted the geoid-height change associated with changes of the Greenland Ice Sheet (Fleming *et al.*, 2004) or the recent retreat of mountain glaciers in Alaska (Tamisiea *et al.*, 2003).

1.5 Objectives

This investigation is concerned with the forward-modelling of present-day rates of geoid-height change and radial displacement due to present and past ice-mass changes in Antarctica. It refines and extends previous studies by employing the most recent models of secular and late Pleistocene/Holocene ice-mass changes and by including a model accounting for seasonal ice-mass changes in Antarctica. The forward-modelling is carried out using the spectral finite-element method developed by Martinec (2000), which includes a consistent treatment of self-gravitation and the sea-level equation (Hagedoorn *et al.*, 2003). The results are discussed with special regard to the GRACE satellite mission and the GPS stations in Antarctica.

Chapter 2 gives an outline of the basic theory by assembling the field equations and interface conditions relevant to GIA modelling and sketching their solution. Moreover, the sea-level equation is explained. Chapter 3 introduces the earth models employed to calculate the elastic-compressible and viscoelastic-incompressible response. For the second case, three viscosity profiles are specified. Chapter 4 describes the load models, which simulate the seasonal and secular ice-mass changes as well as the Pleistocene history of the AIS. Chapter 5 presents the modelling results. For each load model, rates of geoid-height change and radial displacement are presented in the spatial domain. Additionally, degree-power spectra of the rate of geoid-height change are shown. Chapter 6 compares predictions for each load model with observations. In particular, the geoid-height changes are contrasted with preliminary GRACE solutions. The

DOI: 10.2312/GFZ.b103-05011

predicted rates of radial displacement are discussed with reference to estimates of uplift available for the locations of the Antarctic GPS stations and for two Antarctic transects.

DOI: 10.2312/GFZ.b103-05011

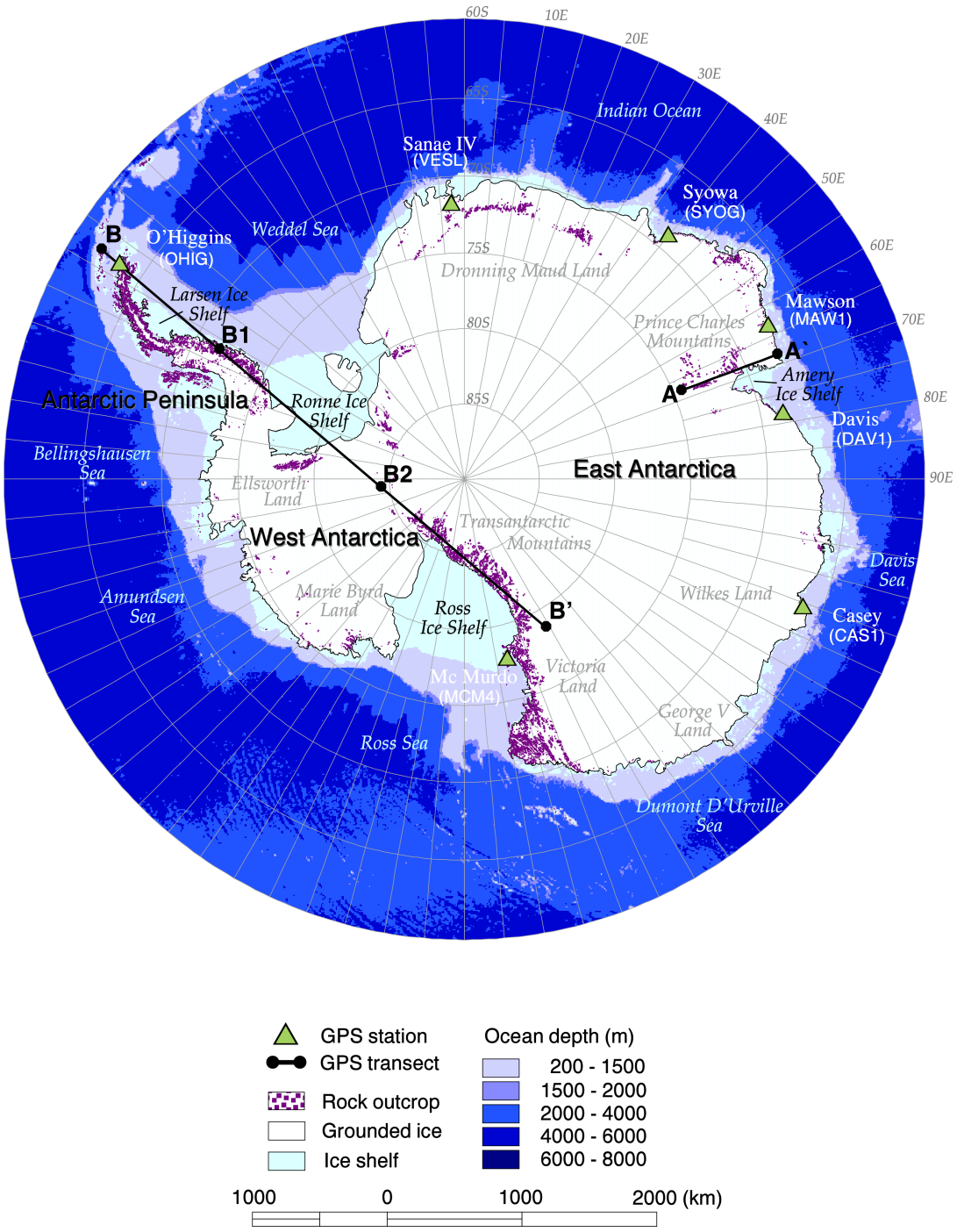

Figure 1.1: Map of Antarctica based on the Antarctica Digital Database (ADD Consortium, 2000 *[online]*), the Digital Chart of the World (ESRI, 2003 *[online]*) and the BEDMAP – bed topography of the Antarctic (Lythe *et al.*, 2000 *[online]*). The toponomy follows the Composite Gazetteer of Antarctica (Cervellati & Geoscience Standing Scientific Group (GSSG), 2003 *[online]*). This and all following maps of Antarctica are in the polar stereographic projection with 0 °E central longitude and 90 °S true-scale latitude.

DOI: 10.2312/GFZ.b103-05011

2

Theory and methods

This chapter outlines the basic theory underlying the computational models employed in this study. In Section 2.1, the field equations and interface conditions relevant to gravitational viscoelastodynamics are formulated according to Wolf (1997, 2003) and Klemann *et al.* (2003). Section 2.2 explains the solution of the field equations based on the spectral finite-element method used for the viscoelastic-incompressible earth model according to Martinec (2000). Section 2.3 outlines the approach adopted for the solution of the sea-level equation according to Hagedoorn *et al.* (2003).

2.1 Field equations and interface conditions of gravitational viscoelastodynamics

Glacial isostasy is concerned with the gravitational-viscoelastic response of the earth to surface loads. To derive the governing incremental field equations and interface conditions, infinitesimal perturbations of a compositionally and entropically stratified, compressible earth initially in hydrostatic equilibrium are assumed in the first instance, with the perturbations taken as isocompositional and isentropic. In the following, the Lagrangian representation of arbitrary tensor fields, $f_{ij\ldots}(\mathbf{X},t)$, will be used, which considers the field values at the current position, $r_i(\mathbf{X},t)$, of a particle whose initial position, X_i, at the time epoch $t=0$ is taken as the spatial argument. The total field, $f_{ij\ldots}(\mathbf{X},t)$, is then decomposed according to $f_{ij\ldots}(\mathbf{X},t) = f^{(0)}_{ij\ldots}(\mathbf{X}) + f^{(\delta)}_{ij\ldots}(\mathbf{X},t)$, where $f^{(0)}_{ij\ldots}(\mathbf{X})$ is the initial field and $f^{(\delta)}_{ij\ldots}(\mathbf{X},t)$ is the material incremental field, i.e. the increment with respect to the particle. Sometimes, it is more convenient to consider the spatial incremental field, i.e. the increment with respect to a fixed location, given by $f^{(\Delta)}_{ij\ldots}(\mathbf{X},t) = f^{(\delta)}_{ij\ldots}(\mathbf{X},t) - f^{(0)}_{ij\ldots,k}(\mathbf{X})u_k(\mathbf{X},t)$, where $u_i(\mathbf{X},t)$ is the particle displacement. For the material gradient of a field, we use $f_{ij\ldots,k}(\mathbf{X},t) := \partial f_{ij\ldots}(\mathbf{X},t)/\partial X_k$. Henceforth, the arguments X_i and t will usually be supressed.

2.1.1 Equations for the total fields

For a self-gravitating earth undergoing quasi-static perturbations of some initial state, the momentum equation is

$$\tau_{ij,j} + \rho^{(0)} g_i = 0, \tag{2.1}$$

where $\tau_{ij,j}$ is the non-symmetric Piola-Kirchhoff stress, $\rho^{(0)}$ the initial volume-mass density and g_i the gravitational force per unit mass. The field g_i is given by

$$g_i = \phi_{,j} b^{-1}_{ji}, \tag{2.2}$$

DOI: 10.2312/GFZ.b103-05011

with ϕ the gravitational potential and b_{ij}^{-1} the inverse of $b_{ij} := r_{i,j}$. The gravitational-potential equation can be written as

$$j(\phi_{,ij} b_{ik}^{-1} b_{jk}^{-1} + \phi_{,i} b_{ik,j}^{-1} b_{jk}^{-1}) = -4\pi G \rho^{(0)}, \tag{2.3}$$

where $j := \det[b_{ij}]$ is the Jacobian determinant and G Newton's gravitational constant. The constitutive equation is of the form

$$t_{ij}(t) = t_{ij}^{(0)} + \mathcal{M}_{ij}[r_{m,k}(t-t')\, r_{m,\ell}(t-t') - \delta_{k\ell}], \tag{2.4}$$

where $t_{ij} = j^{-1} b_{jk} \tau_{ik}$ is the Cauchy stress, $\mathcal{M}_{ij}$ the anisotropic relaxation functional transforming the strain history given by the term in brackets into the current material incremental Cauchy stress, t' the excitation time epoch and δ_{ij} the Kronecker delta. With $\mathcal{M}_{ij}$, $t_{ij}^{(0)}$ and $\rho^{(0)}$ prescribed, (2.1)–(2.4) constitute the system of total field equations for g_i, j, r_i, t_{ij}, τ_{ij} and ϕ.

In order to incorporate loads, the earth is assumed to possess (internal or surficial) interfaces of discontinuity occupied by material sheets whose interface- or surface-mass density, σ, is prescribed. Then, according to Klemann (2003) and Wolf (2003), the following interface conditions result from (2.1)–(2.4):

$$[r_i]_-^+ = 0, \tag{2.5}$$
$$[\phi]_-^+ = 0, \tag{2.6}$$
$$[n_i \phi_{,j} b_{ji}^{-1}]_-^+ = -4\pi G\sigma, \tag{2.7}$$
$$[n_j t_{ij}]_-^+ = -g_i \sigma. \tag{2.8}$$

2.1.2 Equations for the initial fields

Often, the earth can be assumed to be initially in hydrostatic equilibrium, which results in a radially symmetric density distribution. With the mechanical pressure defined by $p := -t_{ii}/3$, then $t_{ij}^{(0)} = -\delta_{ij} p^{(0)}$ applies and (2.1)–(2.4) reduce to

$$-p_{,i}^{(0)} + \rho^{(0)} g_i^{(0)} = 0, \tag{2.9}$$
$$g_i^{(0)} = \phi_{,i}^{(0)}, \tag{2.10}$$
$$\phi_{,ii}^{(0)} = -4\pi G \rho^{(0)}, \tag{2.11}$$
$$p^{(0)} = \xi(\rho^{(0)}, \lambda^{(0)}, \psi^{(0)}). \tag{2.12}$$

The last expression is the state equation, ξ is the state function, $\lambda^{(0)}$ represents the initial composition and $\psi^{(0)}$ is the initial entropy density. With ξ, $\lambda^{(0)}$ and $\psi^{(0)}$ prescribed, (2.9)–(2.12) constitute the system of initial hydrostatic field equations for $g_i^{(0)}$, $p^{(0)}$, $\rho^{(0)}$ and $\phi^{(0)}$.

Supposing $\sigma^{(0)} = 0$, the following initial interface conditions are obtained from (2.5)–(2.8):

$$[r_i^{(0)}]_-^+ = 0, \tag{2.13}$$
$$[\phi^{(0)}]_-^+ = 0, \tag{2.14}$$
$$[n_i^{(0)} \phi_{,i}^{(0)}]_-^+ = 0, \tag{2.15}$$
$$[p^{(0)}]_-^+ = 0. \tag{2.16}$$

DOI: 10.2312/GFZ.b103-05011

2.1.3 Equations for the incremental fields

After decomposition of the total fields in (2.1)–(2.4) into initial and incremental parts followed by linearization with respect to the increments, we obtain, for isotropy,

$$t^{(\delta)}_{ij,j} + (p^{(0)}_{,j} u_j)_{,i} - g^{(0)}_i (\rho^{(0)} u_j)_{,j} + \rho^{(0)} g^{(\Delta)}_i = \rho^{(0)}\, d_t^2 u_i, \tag{2.17}$$

$$g^{(\Delta)}_i = \phi^{(\Delta)}_{,i}, \tag{2.18}$$

$$\phi^{(\Delta)}_{,ii} = 4\pi G (\rho^{(0)} u_i)_{,i}, \tag{2.19}$$

$$\begin{aligned} t^{(\delta)}_{ij} = {} & \delta_{ij} \int_0^t [m_1(t-t') - \tfrac{2}{3} m_2(t-t')]\, d_{t'} [u_{k,k}(t')]\, dt' \\ & + \int_0^t m_2(t-t')\, d_{t'} [u_{i,j}(t') + u_{j,i}(t')]\, dt'. \end{aligned} \tag{2.20}$$

where m_1 and m_2 are the bulk- and shear-relaxation functions, respectively, and d_t is the first-order material time-derivative operator with respect to t. With m_1 and m_2 prescribed and the initial fields given as the special solution to the initial field equations and interface conditions, (2.17)–(2.20) constitute the material-local form of the incremental gravitational-viscoelastic field equations for $g^{(\Delta)}_i$, $t^{(\delta)}_{ij}$, u_i and $\phi^{(\Delta)}$.

Decomposing the total fields in (2.5)–(2.8) into initial and incremental parts followed by linearization gives

$$[u_i]^+_- = 0, \tag{2.21}$$

$$[\phi^{(\Delta)}]^+_- = 0, \tag{2.22}$$

$$[n^{(0)}_i (\phi^{(\Delta)}_{,i} - 4\pi G \rho^{(0)} u_i)]^+_- = -4\pi G \sigma, \tag{2.23}$$

$$[n^{(0)}_j t^{(\delta)}_{ij}]^+_- = -g^{(0)}_i \sigma. \tag{2.24}$$

Before solving (2.17)–(2.20) subject to the interface conditions (2.21)–(2.24), the relaxation functions must be specified. In the following, (2.20) is specialized for elastic-compressible and viscoelastic-incompressible materials.

2.1.4 Elastic-compressible constitutive equation

Partial integration of (2.20) allows us to separate the stress depending on the current time epoch, i.e. the elastic stress, from the stress depending on all previous time epochs, i.e. the viscoelastic stress:

$$\begin{aligned} t^{(\delta)}_{ij} = {} & \delta_{ij} [m_1(0) u_{k,k}(t) - \tfrac{2}{3} m_2(0) u_{k,k}(t) + \tfrac{2}{3} \int_0^t d_{t'} m_2(t-t')\, [u_{k,k}(t')]\, dt'] \\ & + m_2(0)[u_{i,j}(t) + u_{j,i}(t)] - \int_0^t d_{t'} m_2(t-t')\, [u_{i,j}(t') + u_{j,i}(t')] dt'. \end{aligned} \tag{2.25}$$

This expression can be simplified by introducing the linearized strain, $\epsilon_{ij} := (u_{i,j} + u_{j,i})/2$, which can be decomposed according to $\epsilon^{\mathrm{D}}_{ij} := \epsilon_{ij} - \frac{1}{3}\delta_{ij}\epsilon_{kk}$ into deviatoric, $\epsilon^{\mathrm{D}}_{ij}$, and dilatational, $\delta_{ij}\epsilon_{kk}/3$, parts. Then, (2.25) becomes

$$t^{(\delta)}_{ij} = \delta_{ij} m_1(0) \epsilon_{kk} + 2 m_2(0) \epsilon^{\mathrm{D}}_{ij} - 2 \int_0^t d_{t'} m_2(t-t')\, \epsilon^{\mathrm{D}}_{ij}\, dt'. \tag{2.26}$$

DOI: 10.2312/GFZ.b103-05011

On the assumption of perfect elasticity, the viscoelastic stress may be neglected and (2.26) reduces to

$$t_{ij}^{(\delta)} = \delta_{ij} m_1(0) \epsilon_{kk} + 2 m_2(0) \epsilon_{ij}^{\mathrm{D}}, \tag{2.27}$$

where $m_1(0)$ and $m_2(0)$ correspond to the elastic bulk modulus, κ, and elastic shear modulus, μ, respectively.

2.1.5 Viscoelastic-incompressible constitutive equation

The form of (2.20) for incompressibility is obtained if $\epsilon_{kk} \equiv u_{k,k} \to 0$ and $\kappa \to \infty$. Since $t_{ij}^{(\delta)}$ remains finite and the definition of the incremental mechanical pressure, $p^{(\delta)} := -t_{ii}^{(\delta)}/3 = -\kappa \epsilon_{kk}$, continues to apply, (2.26) reduces to (Wolf, 2003)

$$t_{ij}^{(\delta)} = -\delta_{ij} p^{(\delta)} + 2\mu \epsilon_{ij}^{\mathrm{D}} - 2 \int_0^t d_{t'} m_2(t - t') \, \epsilon_{ij}^{\mathrm{D}} \, dt', \tag{2.28}$$

where the the viscoelastic behaviour is controlled by the shear-relaxation function, m_2. Commonly, m_2 is chosen to represent the Maxwell-viscoelastic rheology:

$$m_2(t - t') := \mu e^{-\frac{\mu}{\eta}(t - t')} H(t - t'), \tag{2.29}$$

where η is the shear viscosity and H the Heaviside function[1].

2.2 Solution method

The solution of the field equations and interface conditions for the viscoelastic-incompressible case is carried out following the time-domain spectral finite-element approach by Martinec (2000). In contrast to other solution methods, such as the normal-mode method (e.g. Wu & Peltier, 1982; Peltier, 1985; Han & Wahr, 1995) or the propagator-matrix method (e.g. Wolf, 1985b; Martinec & Wolf, 1998), this approach formulates the initial- and boundary-value problem in a weak sense (e.g. Křížek & Neittaanmäki, 1990), i.e. it imposes the least possible constraints on the properties of the viscosity, elasticity and density distributions. Moreover, the time dependence is formulated as a time-evolution problem, which allows the implementation for arbitrarily changing surface loads considered in the algorithm at each time step. The solution for the elastic-compressible case is based on the standard approach of multiplying the load Love numbers (Farrell, 1972) with the load function, which is detailed in Section A.2. The determination of the load Love numbers is carried out using the Runge-Kutta integrator (e.g. Dahlen & Tromp, 1998).

2.2.1 Time-difference scheme for Maxwell viscoelasticity

First, the time dependence of the viscoelastic-incompressible constitutive equation (2.28) is represented according to a time-difference scheme. The field variables u_i, $t_{ij}^{(\delta)}$, $p^{(\delta)}$ and $\phi^{(\Delta)}$ are represented by their values at discrete time epochs, $t^0 = 0 <$

[1] The Heaviside function of t is defined by $H(t - t') := \begin{cases} 0 \text{ for } t \le t' \\ 1 \text{ for } t > t' \end{cases}$.

DOI: 10.2312/GFZ.b103-05011

$t^1 < ... < t^{t-1} < t^i < t^{i+1}$. With regard to a convenient numerical solution, the explicit Euler time-difference scheme is adopted. Then, the viscoelastic stress at the current time epoch, t^{i+1}, is decomposed into the elastic stress at t^{i+1} and the viscous stress at the previous time epoch, t^i. The time step between two epochs must be chosen sufficiently small to guarantee the stability of the numerical solution.

2.2.2 Weak formulation of the initial- and boundary-value problem

For the reformulation of the initial and interface conditions in a weak sense, the energy functional, $\mathcal{E}$, is defined as the sum of the energy associated with the pressure, $\mathcal{E}_{\text{press}}$, the elastic shear energy, $\mathcal{E}_{\text{shear}}$, the gravitational energy, $\mathcal{E}_{\text{grav}}$, and a term associated with the uniqueness of the solution, $\mathcal{E}_{\text{uniq}}$. The linear functional $\mathcal{F}^{i+1}$ is introduced as the sum of the dissipative part at t^i, $\mathcal{F}^i_{\text{diss}}$, and the part associated with the interface conditions, $\mathcal{F}^{i+1}_{\text{inter}}$. After this, the variational equation for the energy functional and the linear functional is solved for a test function depending on the field variables, u_i, $\phi^{(\Delta)}$ and $p^{(\delta)}$.

2.2.3 Spectral finite-element representation

In the next step, the field variables are expanded into spherical-harmonic functions. For a fixed time epoch, t^{i+1}, the angular dependence of the solution is expressed as vector spherical harmonics for u_i and scalar spherical harmonics for $\phi^{(\Delta)}$ and $p^{(\delta)}$ (Section A.1) and substituted into the variational equation. The radial dependence of the variables is represented by a number of P finite elements with the nodes $0 = r_1 < r_2 < ... < r_P < r_{P+1} = a$.

2.2.4 Galerkin system

After introducing the spectral finite-element representation of the field variables, the Galerkin system is obtained as a system of linear equations for u_i, $\phi^{(\Delta)}$ and $p^{(\delta)}$ and each spherical-harmonic degree and order. The Galerkin method of approximating the solution to the field equations and interface conditions requires a distinct solution for a fixed time epoch, t^{i+1}, such that the variational equation is satisfied. Such a solution for u_i, $\phi^{(\Delta)}$ and $p^{(\delta)}$ is called the spectral finite-element solution.

2.3 Sea-level equation

Glacial changes redistribute mass between the continents and the oceans and induce a viscoelastic response of the earth. The temporal variation of the ice distribution is prescribed by the load model, whereas the distribution of the associated melt water is governed by the sea-level equation (e.g. Johnston, 1993).

The retreat of an ice sheet has various implications for the sea level. In the vicinity of the former ice sheet, the geoid height decreases due to the missing attraction of the former ice masses such that the sea level falls. However, in the areas with ongoing PGR, the influx of mantle material increases the geoid height and, as a consequence, raises the sea level. Furthermore, the melt water entering the oceans also increases the sea level, and, in addition, causes a viscoelastic response. This further changes the geoid height and the sea level and causes a migration of the coastlines.

DOI: 10.2312/GFZ.b103-05011

The following concept of the implementation of the sea-level equation is taken from Hagedoorn *et al.* (2003) and Hagedoorn (2004). The underlying principles are (a) the mass of the ice|ocean system is conserved and (b) the sea level is an equipotential surface. The spatially and temporally varying surface-mass density can be decomposed according to

$$\sigma(\mathbf{\Omega}, t) = \sigma^{\mathrm{I}}(\mathbf{\Omega}, t) + \sigma^{\mathrm{O}}(\mathbf{\Omega}, t) \tag{2.30}$$

into ice and ocean contributions. In the thin-sheet approximation, the ice|ocean surface-mass density $\sigma^{\mathrm{I|O}}$ is given by

$$\sigma^{\mathrm{I|O}}(\mathbf{\Omega}, t) := \rho^{\mathrm{I|O}} s^{\mathrm{I|O}}(\mathbf{\Omega}, t), \tag{2.31}$$

where $\rho^{\mathrm{I|O}}$ is the ice|ocean volume-mass density and $s^{\mathrm{I|O}}$ the ice-|ocean-thickness change. In this study, s^{I} is prescribed by the load model and s^{O} is determined by the sea-level equation:

$$s^{\mathrm{O}}(\mathbf{\Omega}, t) = s^{\mathrm{UF}}(\mathbf{\Omega}, t) + s^{\mathrm{NU}}(\mathbf{\Omega}, t), \tag{2.32}$$

where s^{UF} and s^{NU}, respectively, are the uniform and non-uniform parts of s^{O}. Inverting the spherical-harmonic expansion (A.11):

$$\sigma_{jm}(t) = \int_{\mathbf{\Omega}_0} \sigma(\mathbf{\Omega}, t) Y^*_{jm}(\mathbf{\Omega}) d\mathbf{\Omega}, \tag{2.33}$$

principle (a) takes the form

$$\sigma_{00}(t) = 0, \ t \geq 0. \tag{2.34}$$

The validity of principle (b) is guaranteed by s^{NU}, which takes into account the redistribution of melt water according to the geoid height, e_{G}, and the radial displacement, u_r. The uniform ocean-thickness change, s^{UF}, is equivalent to a water layer of constant thickness distributed over the oceans at the current time epoch, t:

$$s^{\mathrm{UF}}(\mathbf{\Omega}, t) = h^{\mathrm{UF}}(t)\, \mathcal{O}(\mathbf{\Omega}, t), \tag{2.35}$$

with the ocean function, $\mathcal{O}(\mathbf{\Omega}, t)$, defined by

$$\mathcal{O}(\mathbf{\Omega}, t) := \begin{cases} 1, & \text{ocean} \\ 0, & \text{land} \end{cases}. \tag{2.36}$$

The uniform sea-level change, h^{UF}, is given by

$$h^{\mathrm{UF}}(t) = -\frac{\sigma^{\mathrm{I}}_{00}(t) + \sigma^{\mathrm{NU}}_{00}(t)}{\rho^{\mathrm{O}} \mathcal{O}_{00}(t)}, \tag{2.37}$$

where σ^{I}_{00}, $\sigma^{\mathrm{NU}}_{00}$ and $\mathcal{O}_{00}$ are the appropriate expansion coefficients for $j = m = 0$. This equation shows that, in general, s^{UF} and s^{NU} are coupled.

There are several simplifications for the evaluation of the sea-level equation, and the complexity of the approach adopted should be adapted to the scientific objective. In this work, the migration of coastlines is excluded, i.e. $\mathcal{O}(\mathbf{\Omega}, t) = \mathcal{O}(\mathbf{\Omega})$. Moreover,

DOI: 10.2312/GFZ.b103-05011

$s^{\mathrm{NU}}(\mathbf{\Omega}, t)$ is neglected, i.e. the melt water associated with the glacial changes is distributed uniformly over the present-day ocean. A more accurate implementation of the sea-level equation is not required, because the predictions are largely constrained to the continent and the largest part of the sea-level rise caused by the retreat of the Pleistocene ice sheets on the northern hemisphere is excluded in this study. In the future, a more complex implementation will require the adequate treatment of the ice|ocean transition and load models that reflect the grounding-line position of the AIS with greater accuracy. For calculations involving the elastic-compressible earth model, $\mathcal{O}(\mathbf{\Omega}) = 0$ over the grounded portion of the AIS and $\mathcal{O}(\mathbf{\Omega}) = 1$ elsewhere.

With these simplifications,

$$\sigma^{\mathrm{O}}_{jm}(t) = \rho^{\mathrm{O}} h^{\mathrm{UF}}(t) \mathcal{O}_{jm}, \tag{2.38}$$

$$h^{\mathrm{UF}}(t) = -\frac{\sigma^{\mathrm{I}}_{00}(t)}{\rho^{\mathrm{O}} \mathcal{O}_{00}} \tag{2.39}$$

are obtained, where h^{UF} corresponds to the ESL.

DOI: 10.2312/GFZ.b103-05011

3

Earth models

This study predicts the response of the earth to ice-mass variations in Antarctica. Depending on the time scale of the load change, calculations involve either the elastic-compressible or the viscoelastic-incompressible earth model. The seasonal (<1 a) and secular ($\sim$ 100 a) ice-mass changes are regarded as instantaneous and used in conjunction with the elastic-compressible earth model. The consideration of a deglaciation history and the calculation of the associated viscoelastic response requires the application of the more complex viscoelastic-incompressible earth model.

Antarctica consists of two distinct tectonic provinces: East Antarctica is a Precambrian shield, West Antarctica comprises a multitude of younger and tectonically more active terranes. Along the suture zone, uplifted East Antarctic crust forms the Transantarctic Mountains, which also mark a rheological transition that is well established by surface-wave tomography of the upper mantle (Danesi & Morelli, 2001). Across this transition, significant lateral variations in the viscosity stratification and the thickness of the lithosphere are expected, which are ignored when employing a radially symmetric earth model. In this study, three different radial viscosity distributions covering a range of plausible mantle-viscosity values for West and East Antarctica are considered, which allows a crude appraisal of the errors associated with the neglect of lateral heterogeneity.

Section 3.1 introduces the elastic-compressible earth model, which is used in conjunction with the seasonal load models, VAUG and VUNF, and the secular load models, RT02 and VG02. Section 3.2 describes the viscoelastic-incompressible earth model underlying the calculations with the Pleistocene load models, ICE-3G-A and HUY, and introduces three radial viscosity distributions.

3.1 Elastic-compressible earth

The elastic-compressible earth model is used to calculate the earth's response to relatively rapid load changes. It is employed in conjunction with the seasonal load models, VAUG and VUNF (Section 4.1), and the secular load models, RT02 and VG02 (Section 4.2).

The physical parameters incorporated into the earth model are the radial distributions of the volume-mass density, $\rho^{(0)}$, the elastic shear modulus, μ, and elastic bulk modulus, κ (Figure 3.1). Their values are taken from the Preliminary Reference Earth Model (PREM) derived from the analysis of seismic velocities and free oscillations of the earth's body (Dziewonski & Anderson, 1981).

DOI: 10.2312/GFZ.b103-05011

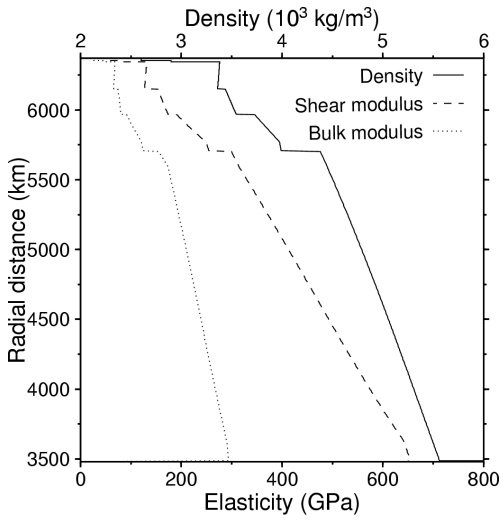

Figure 3.1: Radial density and elasticity distributions according to the PREM (Dziewonski & Anderson, 1981).

3.2 Viscoelastic-incompressible earth

The viscoelastic-incompressible earth model allows us to calculate the present-day GIA of the earth to past load changes. It is used in conjunction with the Pleistocene load models, ICE-3G-A and HUY (Section 4.3).

The viscoelastic response of the earth is mainly influenced by the radial viscosity distribution, which is discretized in three layers of uniform viscosity, i.e. the lithosphere, the upper mantle and the lower mantle. The upper- and lower-mantle viscosities, η^{UM} and η^{LM}, respectively, are considered as the free parameters. As for the elastic earth model, the radial distributions of the volume-mass density, $\rho^{(0)}$, and the elastic shear modulus, μ, are taken from the PREM. The lithosphere is modelled as a layer with a constant thickness of $h^{\mathrm{L}} = 100\,\mathrm{km}$ and a viscosity of $\eta \to \infty$ to behave elastically on the time scale considered. The inner and outer cores are modelled as liquids, $\mu = \eta = 0$, and serve to provide the appropriate interface condition at the core-mantle boundary.

The calculations involve three viscoelastic earth models characterized by increasing values of the upper-mantle viscosity, η^{UM}: the low-viscosity model, LVM, the medium-viscosity model, MP, and the high-viscosity model, HVM (Figure 3.2). The viscosity values of LVM (after Wieczerkowski *et al.*, 1999; Martinec & Wolf, 2004) and MP (after Mitrovica & Peltier, 1989) are based on the analysis of PGR in Fennoscandia. The values of HVM represent an arbitrarily chosen upper limit on reasonable viscosity values for the mantle beneath Antarctica and allow us to place a lower limit on the expected magnitudes of the earth's response. Table 3.1 summarizes the parameters used for the viscoelastic earth models.

It is recognized that the comparison and combination of the results obtained using either the elastic-compressible or the viscoelastic-incompressible earth model is not fully consistent. With regard to the load models, which were developed using various approaches, the most accurate modelling of the earth's response is preferred over a consistent theory. Moreover, Wolf (1985a) showed for a viscoelastic-compressible

DOI: 10.2312/GFZ.b103-05011

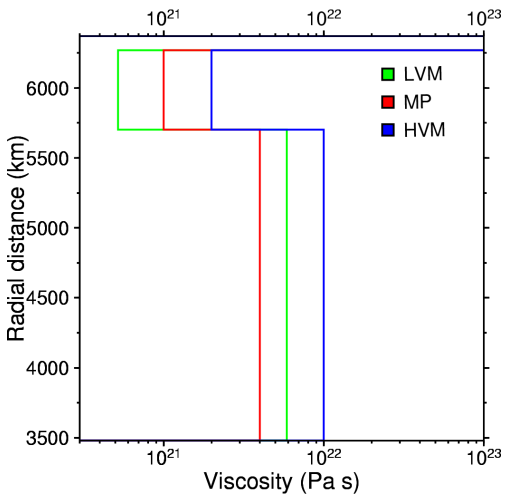

Figure 3.2: Radial viscosity distribution for the viscoelastic earth models LVM, MP and HVM.

Maxwell half-space that the influence of compressibility on the vertical surface displacement associated with PGR is small and decreases with time after emplacement of the load. The author also pointed out that, for times immediately after the emplacement of the load, the surface displacement is rather sensitive to the spatial details of the load distribution, which is not known with great accuracy for Antarctica. It is therefore concluded that, in this study, a viscoelastic-incompressible earth model is appropriate for investigating PGR.

Table 3.1: Parameters of the viscoelastic earth models LVM, MP and HVM.

Model	Lithosphere thickness h^{L} (km)	Viscosity η^{UM} (Pa s)	η^{LM} (Pa s)	Elasticity
LVM	100	5.2×10^{20}	5.9×10^{21}	PREM
MP	100	1.0×10^{21}	4.0×10^{21}	PREM
HVM	100	2.0×10^{21}	1.0×10^{22}	PREM

DOI: 10.2312/GFZ.b103-05011

4

Load models

In this study, the earth's response to present and past changes of the AIS is calculated. These changes are described by load models, which provide the spatial ice-thickness distribution at the time epoch considered with respect to the distribution at present.

So far, there has been developed no model of the AIS that describes its evolution in a consistent manner. Individual studies typically investigated one particular aspect of the ice sheet, e.g. the LGM or the present-day state, the dynamics of the ice sheet during the glacial cycles or the behaviour of individual glaciers and ice streams at present. The results are usually approximate, which is largely due to the rather weak constraints imposed by scarce and sometimes ambiguous field evidence.

This study uses the results from various investigations to construct load models describing the thickness changes of the ice sheet on seasonal (< 1 a) or secular (~ 100 a) time scales as well as its deglaciation history since the LGM. For each time scale, two distinct load models allow us to examine the sensitivity of the results to their particular features.

Section 4.1 introduces the seasonal load models VAUG based on accumulation measurements and VUNF assuming uniform accumulation. Section 4.2 details the secular load models RT02, which is based on mass-balance data for drainage basins, and VG02, which adopts the pattern of accumulation data used for VAUG. Section 4.3 describes the Pleistocene load models, ICE-3G-A and HUY. ICE-3G-A is based on geomorphological evidence and has gained (despite known flaws) the status of a reference model. In contrast to this, HUY is based on the results of recent numerical modelling.

4.1 Seasonal ice-mass balance

The seasonal load models, VAUG and VUNF, describe the annual variation of the ice thickness of the grounded portion of the AIS. They are constructed from an estimate of the annual snow accumulation (Vaughan *et al.*, 1999) and an appraisal of the Antarctic contribution to the seasonal variation of the global mean sea level (Cazenave *et al.*, 2000).

For most of the AIS, surface melting is of minor importance (the Antarctic Peninsula is an exception). Most of the annual snow fall is assimilated by the ice sheet and transported via ice streams and outlet glaciers to the ice shelves, where it is eventually discharged. Vaughan *et al.* (1999) termed this annual flux of snow into the ice sheet the net surface-mass balance.

The net surface-mass balance is zero for areas of rock outcrops and bare ice, also called blue ice, which tend to be small in size. The most important site of bare ice is

DOI: 10.2312/GFZ.b103-05011

part of the Lambert Glacier in East Antarctica, where the net surface-mass balance is zero over an area of $56 \times 10^3\,\mathrm{km}^2$, corresponding to 4 % of the area of the drainage basin Lambert/Mellor/F (LAM in Figure 4.3).

The seasonal load models, VAUG and VUNF, consist of two components: the spatial pattern of the net surface-mass balance, which is distinct for both models, and the temporal variation of the total ice mass and the associated global mean sea level based on Cazenave *et al.* (2000), which is identical for both models.

Cazenave *et al.* (2000) analyzed the seasonal variation of the global mean sea level determined from a 6 a time series of Topex-Poseidon satellite-altimetry data. The results indicate that the annual variability of the Antarctic sea-level contribution has a magnitude of 5.6 mm ESL and varies approximately sinusoidally, showing a maximum on December 30. The corresponding variation of the total ice-mass change adopted for the seasonal load models is considered as anti-cyclical to the variation of the sea-level (Figure 4.2).

In Sections 4.1.1 and 4.1.2, the spatial patterns of the net surface-mass balances employed for load models VAUG and VUNF are described. All values represent the annual variability, i.e. the double amplitude of the sinusoidal annual variation of the ice-thickness or the corresponding ESL change, which is referred to as the seasonal variation.

4.1.1 VAUG: in situ accumulation measurements

Load model VAUG describes the seasonal variation of the AIS based on the spatial pattern of the net surface-mass balance published by Vaughan *et al.* (1999). The authors included 1860 irregularly distributed in situ measurements of the net surface-mass balance and interpolated the data using a strongly correlated background field of higher coverage derived from passive-microwave satellite observations.

For load model VAUG, the spatial pattern is assumed to represent the maximum ice-thickness change due to annual accumulation, occurring between January and July (Figure 4.1). The value of the associated sea-level change taken from Vaughan *et al.* (1999) amounts to −4.9 mm ESL, which is a slightly smaller seasonal variation than the −5.6 mm ESL proposed by Cazenave *et al.* (2000).

Load model VAUG is characterized by large ice-thickness changes in the coastal regions. Extreme values of up to 825 mm are found along the Antarctic Peninsula, in Ellsworth Land (West Antarctica) and Wilkes Land (East Antarctica). Extensive areas of central and East Antarctica show a moderate ice-thickness change close to 124 mm. Areas along the coast, where changes exceed 124 mm, contribute 530 Gt or −1.5 mm ESL to the seasonal variation of the total ice mass.

4.1.2 VUNF: uniform accumulation

Load model VUNF describes the seasonal variation of the AIS assuming a uniform spatial pattern of the net surface-mass balance.

In the interpolation of Vaughan *et al.* (1999), used in load model VAUG, large parts of central and East Antarctica exhibit moderate ice-thickness changes close to 124 mm. An extrapolation of this value to the rest of the grounded ice sheet yields a total ice-mass change of 1270 Gt or −3.4 mm ESL. A comparison with load model VUNF allows us in particular to assess the importance of the seasonal changes in the coastal regions.

DOI: 10.2312/GFZ.b103-05011

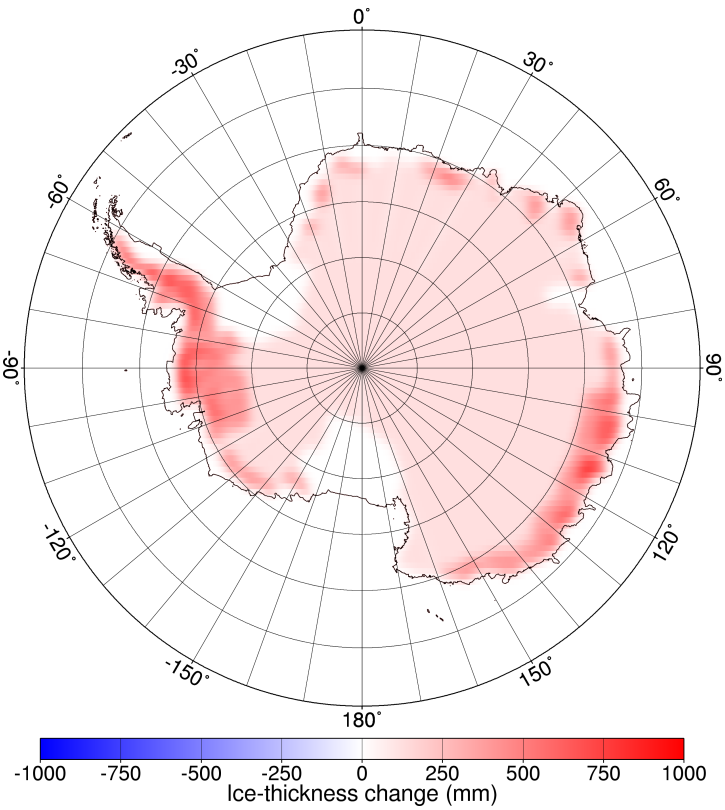

Figure 4.1: Ice-thickness change of the seasonal load model VAUG (after Vaughan *et al.*, 1999). Changes are due to snow accumulation between January and July (Figure 4.2). Strongest accumulation occurs in the coastal regions, particularly along the Antarctic Peninsula, in Ellsworth Land and Wilkes Land. Accumulation is moderate and more uniform in the interior of Antarctica. The discretization is $0.25° \times 0.25°$.

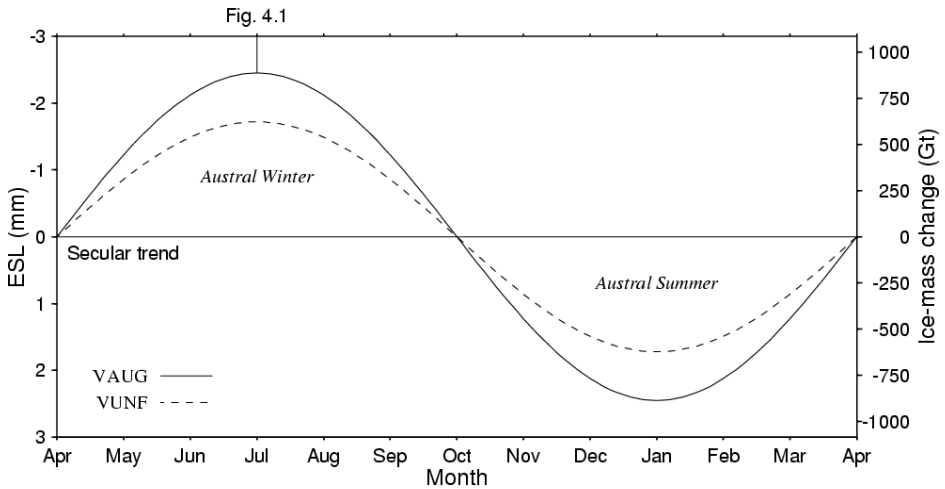

Figure 4.2: Total ice-mass variation of the seasonal load models VAUG and VUNF (after Cazenave *et al.*, 2000). Accumulation occurs from January to July, discharge occurs from August to December. The maximum ice thickness shown in Figure 4.1 is reached at the end of July (austral winter). Accumulation and discharge are in balance, i.e. the secular trend of the total ice-mass change is zero.

DOI: 10.2312/GFZ.b103-05011

4.2 Secular ice-mass balance

The secular load models, RT02 and VG02, describe interannual changes of the AIS, which represent a long-term contribution to global mean sea-level change.

As mentioned in Section 1.4, previous GIA studies of Antarctica mainly employed the secular load models S1, S2 by mass, S2 by area and J92, primarily developed by James & Ivins (1997) (e.g. James & Ivins, 1998; Kaufmann, 2002). The range of models reflects the inaccuracy and scarcity of the mass-balance data available at that time and involve total ice-mass changes from $-1.1\,\mathrm{mm/a\,ESL}$ (S2 by mass) to $0.45\,\mathrm{mm/a\,ESL}$ (J92).

Since then, the reliability and coverage of mass-balance data has increased chiefly due to the application of remote-sensing techniques. A recent review by Rignot & Thomas (2002) indicates that the AIS is roughly in balance and contributes merely $(0.07 \pm 0.07)\,\mathrm{mm/a\,ESL}$[1] to the global mean sea-level rise.

Load models RT02 and VG02 feature two contrasting spatial patterns of ice-thickness change. RT02, described in Section 4.2.1, is constructed from the mass-balance data of drainage basins published by Rignot & Thomas (2002). VG02, explained in Section 4.2.2, uses the accumulation data underlying the seasonal load model VAUG.

4.2.1 RT02: mass balance of drainage basins

The secular load model RT02 describes the rate of ice-thickness change for 33 Antarctic drainage basins (Figure 4.3). It is constructed from the bulk mass balance of each drainage basin calculated as the difference between annual accumulation and discharge published by Rignot & Thomas (2002).

Rignot & Thomas (2002) determined the accumulation for each drainage basin from an assessment of the net surface-mass balance by Giovinetto & Zwally (2000), which is similar to the one underlying the seasonal load model VAUG developed by Vaughan *et al.* (1999). The discharge values are based on various measurement approaches, for instance satellite altimetry determining surface-elevation changes, or Interferometric Synthetic-Aperture Radar (InSAR) indicating ice-flow velocities and grounding-line positions.

Table 4.1 summarizes the mass-balance data for the 33 drainage basins considered. The data cover 75 % of West Antarctica, 55 % of East Antarctica and include 25 of the 30 drainage basins known to have major mass fluxes. Load model RT02 assumes a spatially averaged rate of ice-thickness change, $<\dot{s}^{\mathrm{I}}>$, for the entire area of the drainage basin, which is calculated from the rate of total ice-mass change and the area of the drainage basin according to Rignot & Thomas (2002). Regions not considered are assumed to be in balance, i.e. $<\dot{s}^{\mathrm{I}}> = 0$.

Figure 4.3 shows the spatial pattern of $<\dot{s}^{\mathrm{I}}>$ described by RT02. For West Antarctica, large variations of $<\dot{s}^{\mathrm{I}}>$ ($\sim 100\,\mathrm{mm/a}$) occur on a small spatial scale ($< 500\,\mathrm{km}$). Maximum thickening of 143 mm/a is associated with the abrupt deceleration of Ice Stream C (C)[2] observed during the last decade (Rignot & Thomas, 2002). Extreme values of thinning, ranging from -547 to $-875\,\mathrm{mm/a}$, are found for the glaciers draining into the Amundsen Sea, i.e. Smith (SMI), Kohler (KOH), De Vicq

[1] The error is calculated from the errors for West and East Antarctica provided by Rignot & Thomas (2002).

[2] Text tokens in brackets refer to the drainage-basin IDs used in Table 4.1 and Figure 4.3.

DOI: 10.2312/GFZ.b103-05011

(DVQ) and Land (LAN). The average rate of ice-thickness change for West Antarctica is −30 mm/a. The corresponding total ice-mass change amounts to −45 Gt/a or 0.12 mm/a ESL.

For East Antarctica, the ice thickness generally increases. Compared to West Antarctica, variations of $<\dot{s}^{\mathrm{I}}>$ are about one order of magnitude lower (~ 10 mm/a) and occur on a broader spatial scale (> 500 km). Maximum thickening of 17 mm/a is found for the Byrd Glacier (BYR), maximum thinning of −17 mm/a applies to the Stancomb-Wills Ice Stream (STA). The average rate of ice-thickness change for East Antarctica is 4 mm/a. The associated total cahnge of mass equals 19 Gt/a or −0.05 mm/a ESL.

The mass-balance data of Rignot & Thomas (2002) do not include measurements on several glaciers in the Transantarctic Mountains and the Support-Force Ice Stream, which is located between the Recovery Glacier (REC) and Foundation Ice Stream (FOU). Moreover, according to Rignot & Thomas (2002), significant uncertainties of the mass-balance data for East Antarctica are due to the poor determination of the divide between the Foundation (FOU) and the Support-Force Ice Stream. Furthermore, insufficient satellite coverage in the area south of 81.5 °S leads to unreliable mass-balance estimates for drainage basins close to the pole, e.g. the Byrd Glacier (BYR). As a consequence, estimates of the total ice-mass change for East Antarctica range from −0.11 to 0.01 mm/a ESL. For West Antarctica, the data have higher coverage and are more accurate, a consequence being that the estimated total ice-mass change can be bracketed between 0.09 and 0.16 mm/a ESL.

Rignot & Thomas (2002) excluded mass-balance data for the Antarctic Peninsula. Although this region represents merely 7% of the Antarctic continent, it receives roughly one quarter of the total annual precipitation and is therefore likely to contribute significantly to the Antarctic ice-mass budget. Its proximity to the ocean and its extent to low latitudes destines its ice reservoirs to be most sensitive to climate changes. During the last 50 a, a strong regional warming of 2 to 3 °C has resulted in enhanced thinning and melting of the mountain glaciers and rapid disintegration of the ice shelves (Vaughan *et al.*, 2001). It continues to be debated whether ice shelves stabilize their tributary glaciers. If so, the disintegration of ice shelves leads to accelerated flow of the glaciers, and the Antarctic Peninsula will play a crucial role in the assessment of climate-induced changes of the global mean sea level.

4.2.2 VG02: seasonal imbalance of load model VAUG

The secular load model VG02 describes the interannual trend arising from a possible imbalance between annual accumulation and discharge for the seasonal load model VAUG. It adopts the spatial pattern of the net surface-mass balance used in VAUG (Vaughan *et al.*, 1999), but adjusts the secular trend of the total ice-mass change to −25 Gt/a or 0.07 mm/a ESL, which is the value adopted in RT02. The values of $\dot{s}^{\mathrm{I}}$ for this model are proportional to the values of s^{I} for load model VAUG by a factor of $-0.014\,\mathrm{a}^{-1}$.

DOI: 10.2312/GFZ.b103-05011

Table 4.1: Mass balance of drainage basins in Antarctica (Rignot & Thomas, 2002). Data cover 58 % of Antarctica (75 % of West Antarctica, 55 % of East Antarctica) and include 25 of the 30 drainage basins with major mass fluxes. In total, Antarctica loses mass corresponding to 0.07 mm/a ESL. Error estimates for each drainage basin are given in the original publication, but are not considered in this study.

Drainage basin		Area	$\dot{m}$	$<\dot{s}^{\mathrm{I}}>$	$\dot{h}^{\mathrm{O}}$
ID	Name	(10^3 km^2)	(Gt/a)	(mm/a)	(mm/a ESL)
PIG	Pine Island	162.3	−7	−49.3	0.02
THW	Thwaites	164.8	−21	−139.6	0.06
SMI	Smith	16.5	−12	−787.9	0.03
KOH	Kohler	10.2	−6	−686.3	0.02
DVQ	DeVicq	16.0	−13	−875.0	0.04
LAN	Land	12.8	−6	−546.9	0.02
A/WHI	A/Whillans	235.2	5	21.3	−0.01
C	C	153.4	20	143.4	−0.05
D	D	140.3	4	28.5	−0.01
E	E	175.2	1	5.7	0.00
F	F	16.8	1	59.5	0.00
EVA	Evans	108.4	−5	−46.1	0.01
CAR	Carslon	9.1	0	0.0	0.00
RUT	Rutford	52.6	0	0.0	0.00
INS	Institute	166.9	−1	−6.0	0.00
FOU	Foundation	221.6	−4	−18.1	0.01
Subtotal	West Antarctica (75 %)	1662.1	−45	−29.5	0.12
BAI	Bailey	66.7	0	0.0	0.00
SLE	Slessor	499.2	1	2.0	0.00
REC	Recovery	964.3	4	4.1	−0.01
DAV	David	214.3	−2	−9.3	0.01
COO	Cook Ice Shelf	107.9	0	0.0	0.00
NIN	Ninnis	170.8	4	23.4	−0.01
MER	Mertz	82.6	2	24.2	−0.01
TOT	Totten	537.9	−7	−14.9	0.02
DEN	Denman	186.3	1	5.4	0.00
SCO	Scott	29.5	0	0.0	0.00
LAM	Lambert/Mellor/F	953.7	−3	−3.1	0.01
RAY	Rayner	104.0	0	0.0	0.00
SHI	Shirase	196.7	2	10.2	−0.01
JUT	Jutulstraumen	122.5	0	0.0	0.00
STA	Stancomb-Wills	99.9	−2	−20.0	0.01
BYR	Byrd	1070.4	19	19.6	−0.05
MUL	Mulock	115.0	1	8.7	0.00
Subtotal	East Antarctica (55 %)	5521.7	19	3.8	−0.05
Total	Antarctica (58 %)	7183.8	−25	−3.9	0.07

DOI: 10.2312/GFZ.b103-05011

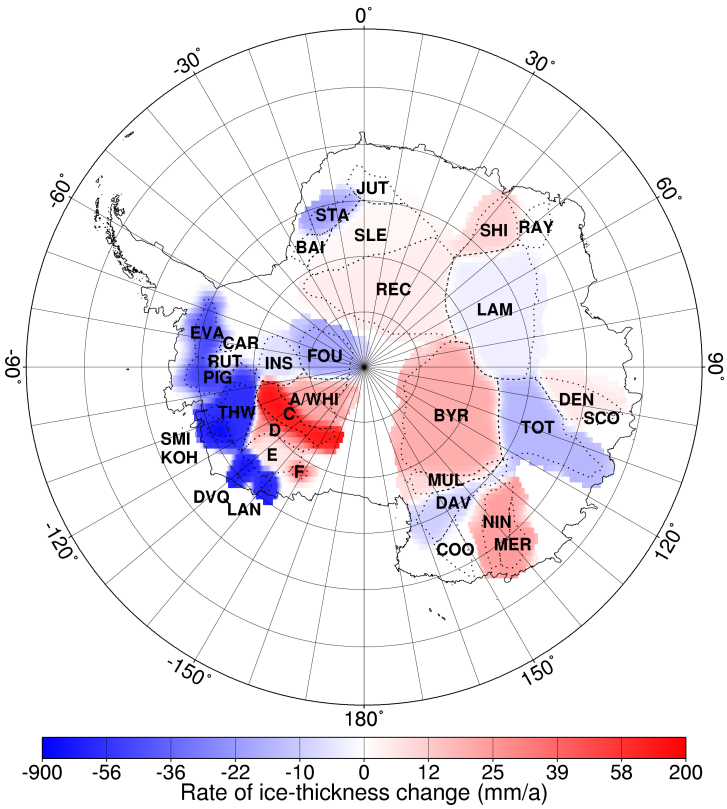

Figure 4.3: Rate of ice-thickness change for the secular load model RT02 (after Rignot & Thomas, 2002). Dotted lines divide the AIS into 33 drainage basins. The mass balance of each drainage basin is described by an average rate of ice-thickness change, $<\dot{s}^{\mathrm{I}}>$, listed in Table 4.1. West Antarctica exhibits the largest values of $<\dot{s}^{\mathrm{I}}>$ for the glaciers in the coastal regions (drainage basins THW, SMI, KOH, DVQ and LAN) and the ice streams entering the Ross Ice Shelf (drainage basins A/WHI and C−F). For East Antarctica, the drainage basins are more balanced. The total secular ice-mass change is $-25\,\mathrm{Gt/a}$ or $0.07\,\mathrm{mm/a\,ESL}$. The discretization is $0.25° \times 0.25°$.
The abbreviations for the drainage basins are: Pine (PIG), Thwaites (THW), Smith (SMI), Kohler (KOH), DeVicq (DVQ), Land (LAN), A/Whillans (A/WHI), Ice Stream C−F (C−F), Evans (EVA), Carslon (CAR), Rutford (RUT), Institute (INS), Foundation (FOU), Bailey (BAI), Slessor (SLE), Recovery (REC), David (DAV), Cook (COO), Ninnis (NIN), Mertz (MER), Totten (TOT), Denman (DEN), Scott (SCO), Lambert/Mellor/F (LAM), Rayner (RAY), Shirase (SHI), Jutulstraumen (JUT), Stancomb-Wills (STA), Byrd (BYR) and Mulock (MUL).

DOI: 10.2312/GFZ.b103-05011

4.3 Pleistocene deglaciation

The state of the AIS at the LGM and the timing of its successive disintegration are not satisfactorily known. Field evidence constrains the maximum extent of the ice sheet. However, the retreat history and the ice distribution on a regional scale are difficult to assess. Constraints are primarily derived from five approaches: (a) geomorphological evidence (such as moraines, depositional and erosional limits and the distribution of erratics), (b) the analysis of GIA (Section 1.1), (c) numerical modelling, (d) the analysis of RSL data and (e) ice-core analysis.

In the past, various deglaciation models for Antarctica were proposed and applied to GIA investigations, e.g. ANT3 (Nakada & Lambeck, 1988), a numerical model (Huybrechts, 1990), D91 (Denton *et al.*, 1991) and ICE-3G (Tushingham & Peltier, 1991). Large differences between the models exist for the amount of additional ice at the LGM and its spatial distribution (e.g. Anderson *et al.*, 2002). Common to the models is the rather large additional ice mass at the LGM. For instance, ICE-3G has an additional mass corresponding to −25 m ESL, whereas the values for the other models range between −12 m ESL (Huybrechts, 1990) and −37 m ESL (Nakada & Lambeck, 1988).

More recently, Bentley (1999) reviewed the constraints imposed by the individual approaches and concluded that the AIS contained significantly less additional ice at the LGM than previously proposed, suggesting values between −6.1 and −13.1 m ESL. This reduction is supported by modelling studies due to Denton & Hughes (2002) and Huybrechts (2002), who proposed 'best estimates' of −14 and −17.5 m ESL, respectively.

There is consent that the additional ice was mainly stored in the regions of today's major ice shelves of West Antarctica and the Antarctic Peninsula, although the exact amount is unclear. For instance, Bentley (1999) attributed −2.3 to −3.2 m ESL to the Ross Ice Shelf, −1.7 m ESL to the Larsen Ice Shelf and −2.7 m ESL to the Ronne Ice Shelf. Field evidence not only indicates independent retreat histories for East and West Antarctica, but also a different timing of the deglaciation of the ice shelves (Anderson *et al.*, 2002).

The present study uses two deglaciation models, ICE-3G-A and HUY, detailed in the following two sections. ICE-3G-A adapts the global reconstruction of the Pleistocene deglaciation by Tushingham & Peltier (1991), which is based on geomorphological and RSL data. HUY is based on numerical modelling by Huybrechts (2002). For the ease of comparison, both models are adjusted to hold additional ice corresponding to −12 m ESL at the LGM, which is within the range estimated by Bentley (1999).

4.3.1 ICE-3G-A: geomorphological model

The Pleistocene load model ICE-3G-A describes the disintegration of the AIS from the LGM to the present time. The spatial ice distribution at the LGM and the timing of its retreat are taken from the Antarctic component of the global Pleistocene load model ICE-3G developed by Tushingham & Peltier (1991).

The original model of Tushingham & Peltier (1991) describes the spatial ice distribution by means of 808 disc loads of various thicknesses and radii. The thicknesses of the discs are changed to a new configuration every 1000 a, starting at the end of the LGM. The parameters of the disc loads are optimized in an iterative process in

DOI: 10.2312/GFZ.b103-05011

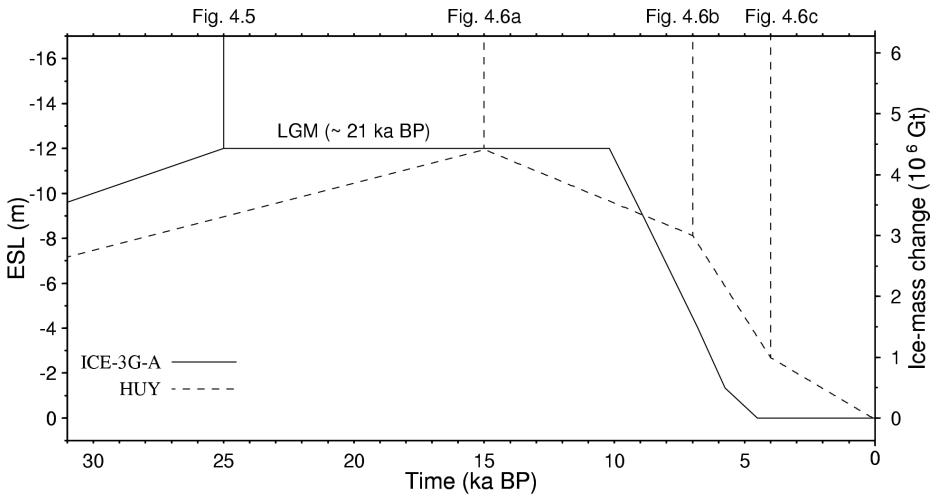

Figure 4.4: Total ice-mass change for the Pleistocene load models ICE-3G-A and HUY. Both models have a glaciation phase, which starts at 55 ka BP and eventually adds -12 m ESL or 4.3×10^6 Gt of ice to the AIS. ICE-3G-A sustains the LGM state between 25 and 10.2 ka BP and then turns into a rapid deglaciation phase ceasing at 4.5 ka BP. The spatial ice distribution is constant during deglaciation (Figure 4.5). HUY reaches the LGM state at 15 ka BP and features a deglaciation phase, with particularly fast changes between 7 and 4 ka BP, continuing to the present. The spatial ice distribution is variable (Figure 4.6).

order to maximize the agreement between predictions and observations of RSL at selected locations distributed over the earth. A basic simplification underlying the construction of ICE-3G is the radial symmetry of the earth model employed.

For the present purposes, ICE-3G is adapted to the regional study of Antarctica. The deglaciation model ICE-3G-A used only considers ice-mass changes south of 60 °S, which are implemented as a gridded data set rather than as parameters of disc loads. Values of the ice-thickness change are multiplied by a factor of 0.45 to give -12 m-ESL additional total ice mass at the LGM instead of the original -25 m ESL. However, the modified model inherits the timing of the deglaciation history according to Tushingham & Peltier (1991) shown in Figure 4.4. As in the original model, the spatial distribution of the relative ice-thickness change is constant during deglaciation (Figure 4.5).

4.3.2 HUY: numerical model

The Pleistocene load model HUY is used as an alternative to ICE-3G-A. It is based on the results of thermomechanical modelling by Huybrechts (2002). In contrast to ICE-3G-A, load model HUY features distinct spatial ice distributions at 15, 7 and 4 ka BP and, hence, allows for a regional retreat history.

In his study, Huybrechts (2002) simulated the variation of the volume and extent of the AIS during the last four glacial cycles, starting $\sim$400 ka BP. His thermomechanical model is mainly forced by two paleo-environmental parameters: the surface temperature, derived from the δD hydrogen-isotope record of the Vostok ice core in East Antarctica, and the eustatic sea-level change, inferred from marine δ^{18}O oxygen-

DOI: 10.2312/GFZ.b103-05011

isotope records. The surface temperature is transformed into precipitation and basal-melting rates using relationships established from present-day observations. Another key parameter controlling the ice volume at the LGM as well as the ice extent during deglaciation is the bedrock elevation and its changes due to GIA. For instance, the extent of the western part of the AIS at the LGM is largely constrained by the continental margin (Figure 1.1).

Load model HUY is linearly interpolated from four snapshots of the AIS according to Huybrechts (2002), which display the surface elevation in reference to the present-day sea level at 15, 7, 4 ka BP and present day. The images are digitized and gridded. Then, differences between the three past states and the present-day state are calculated. Finally, the spatial pattern of the ice-thickness change is approximated by scaling the spatial pattern of the surface-elevation change to the total ice-mass change adopted. Figure 4.4 shows the ice-mass change since the LGM, whereas Figure 4.6 shows the ice-thickness changes since 15, 7 and 4 ka BP.

In load model HUY, bedrock-elevation changes present in the underlying snapshots of the AIS are not considered, and the surface-elevation change is taken as proxy for the ice-thickness change. Since the lithosphere acts as a low-pass filter (e.g. Wu & Peltier, 1982; Wolf, 1984, 1985b), this simplification only affects the longest wavelenghts of the ice-thickness change in load model HUY.

DOI: 10.2312/GFZ.b103-05011

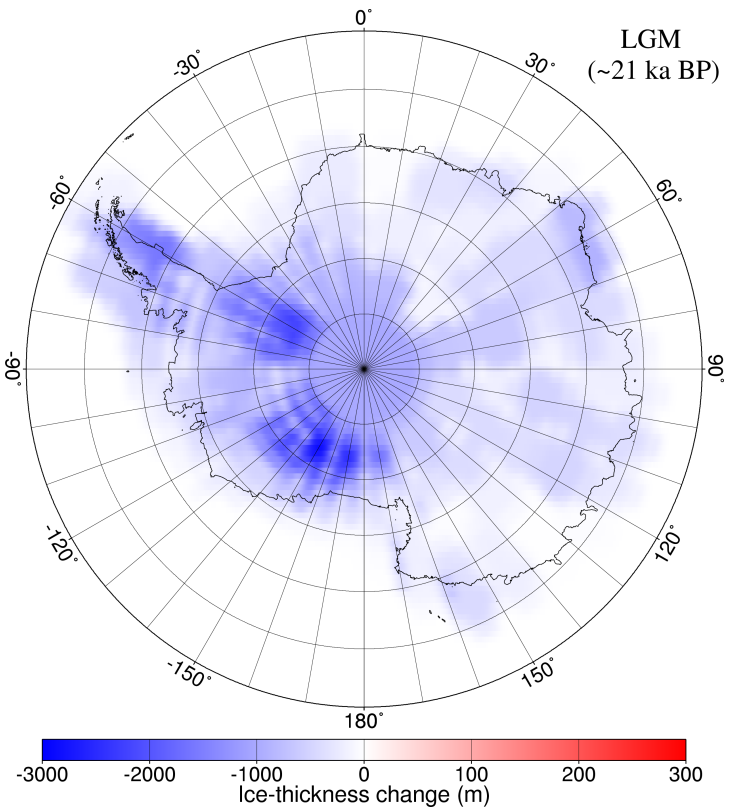

Figure 4.5: Ice-thickness change since the LGM for the Pleistocene load model ICE-3G-A (after Tushingham & Peltier, 1991). Largest changes occur on the present major ice shelves of West Antarctica and the Antarctic Peninsula: the Ross, Ronne and Larsen Ice Shelves. The spatial distribution of the relative ice-thickness change is constant during deglaciation. The discretization is $0.25° \times 0.25°$.

DOI: 10.2312/GFZ.b103-05011

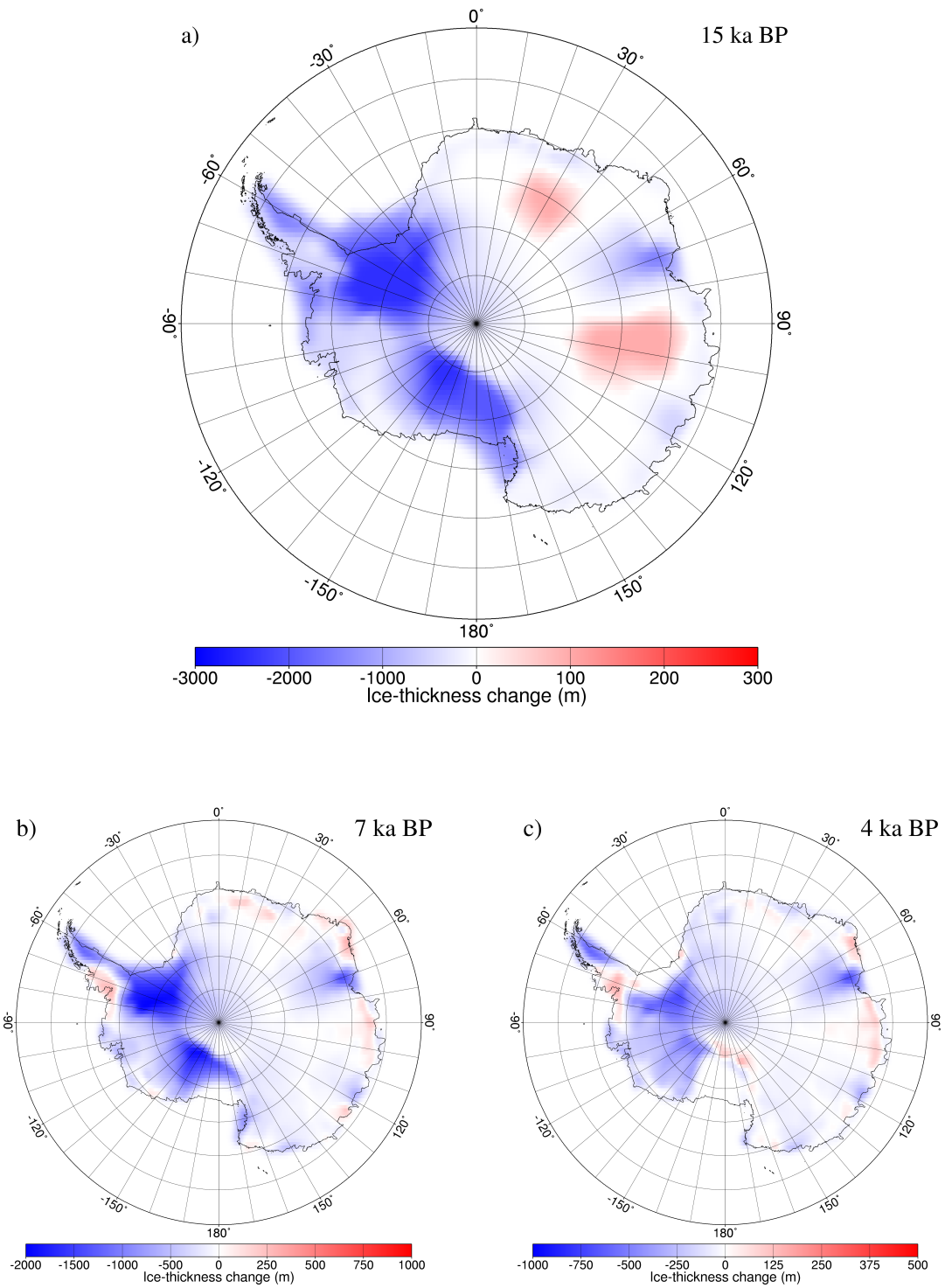

Figure 4.6: Ice-thickness change since 15, 7 and 4 ka BP for the Pleistocene load model HUY. (a) 15 ka BP: Largest changes occur on the Ross, Ronne, Larsen and Amery Ice Shelves, central parts of East Antarctica show a slight increase of ice. (b) 7 ka BP: Grounded ice has largely retreated from today's Ross Ice Shelf. (c) 4 ka BP: The Ronne Ice Shelf still experiences important deglaciation after 4 ka BP. The discretization is $0.25° \times 0.25°$.

DOI: 10.2312/GFZ.b103-05011

5

Results

This chapter presents the results of the predictions for the various load models. Section 5.1 addresses the seasonal ice-mass balance, Section 5.2 the secular ice-mass balance and Section 5.3 the Pleistocene deglaciation. For the corresponding load models, first the results for the geoid-height change in the spectral and spatial domains are introduced, then the radial displacement is calculated. The spectra of the geoid-height change are shown as degree-power spectra (Section A.1) and compared to an estimate of the GRACE accuracy (Wahr & Velicogna, 2003). The geoid-height change is calculated from the gravitational potential (Section 2.1.3) according to (A.7).

5.1 Seasonal ice-mass balance

This section presents the elastic-compressible earth response to the seasonal load models VAUG and VUNF. In Section 5.1.1, predictions for the spectral geoid height are presented as degree-power spectra, Section 5.1.2 addresses the spatial geoid height. The radial displacement with respect to the permanent GPS stations is shown in Section 5.1.3.

The load models represent the geoid height and radial displacement, e_{G} and u_r, respectively, due to the snow accumulation on the AIS between January and July. The values for load model VAUG, which is considered as more realistic, also provide an estimate of the annual variation of the secular trends, $\dot{e}_{\mathrm{G}}$ and $\dot{u}_r$. The predictions for this model are called the seasonal variability, $e_{\mathrm{G}}^{\mathrm{VAUG}}$ and u_r^{VAUG}.

5.1.1 Spectral geoid-height change

VAUG

The spectral geoid height for load model VAUG shows magnitudes well above the estimated GRACE accuracy (Figure 5.1). The spectrum has high power even at high degrees, which reflects the large total ice-mass change involved ($-4.9\,\mathrm{mm/a\,ESL}$), of which about one third can be attributed to changes within a narrow fringe along the coast. With increasing degree, the magnitude decreases from $6 \times 10^{-1}\,\mathrm{mm}$ for degree 2 (maximum) to $7 \times 10^{-3}\,\mathrm{mm}$ for degree 64. The power distribution for the coefficients exhibits characteristic highs every 5 to 6 degrees, which is due to the boundary imposed by the Antarctic coastline.

VUNF

The uniform load model VUNF produces a spectral geoid height with an overall power distribution similar to VAUG, ranging between $4 \times 10^{-1}\,\mathrm{mm}$ for degree 2 and $2 \times 10^{-3}\,\mathrm{mm}$ for degree 64 (Figure 5.1). Up to degree 9, load models VUNF and

DOI: 10.2312/GFZ.b103-05011

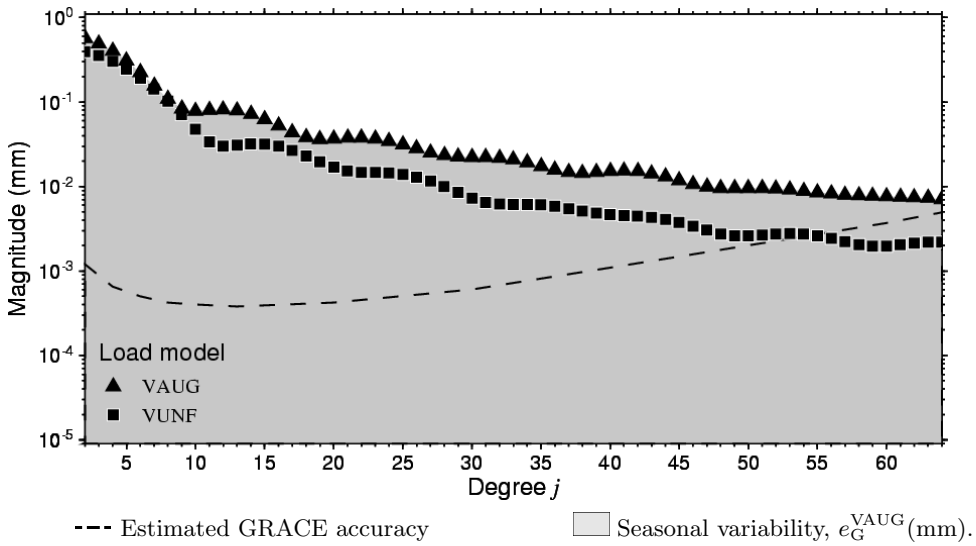

Figure 5.1: Degree-power spectrum of e_G for the seasonal load models VAUG and VUNF and the elastic-compressible earth model.

VAUG produce approximately the same signature. However, at higher degrees, the magnitudes for VUNF are reduced, which is caused by the lack of small-scale and high-magnitude ice-thickness changes in the coastal regions.

5.1.2 Spatial geoid-height change

VAUG

In the spatial domain, load model VAUG produces a geoid height of up to 10 mm and is generally greater than 1.5 mm south of 60 °S (Figure 5.2 a). The 4.5 mm isoline encompasses most of the Antarctic continent. Extreme values of e_G occur over the coastal areas where the accumulation is highest: the Antarctic Peninsula, Ellsworth Land and Wilkes Land. Further inland and over most of central and East Antarctica, the geoid height is between 6 and 7 mm. A local maximum of 8 mm is located near Vostok Station, East Antarctica (106.80 °E, 78.45 °S).

VUNF

Load model VUNF, describing a uniform ice-thickness change of 124 mm, causes a geoid height of up to 7 mm, with changes south of 60 °S generally greater than 1.2 mm. Over the central parts of the continent, the spatial pattern is very similar to the one for VAUG. However, in contrast to VAUG, the values decrease continuously toward the coast. The 3.9 mm isoline encompasses most of the Antarctic continent, but excludes the tip of the Antarctic Peninsula. The maximum of 7 mm is located close to Vostok Station, where a local maximum is obtained for load model VAUG. The differences in the geoid height for load models VAUG and VUNF are confined to the coastal regions and on the order of several mm.

DOI: 10.2312/GFZ.b103-05011

5.1.3 Radial displacement

VAUG

The spatial pattern of the radial displacement for load model VAUG is shown in Figure 5.2 b. The −5 mm isoline generally follows the coastline. An exception is the tip of the Antarctica Peninsula, where the radial displacement is only −2 to −4 mm. Extreme displacements of up to −16 mm are found along the Antarctic Peninsula, in Ellsworth Land and Wilkes Land. For most of central and East Antarctica, the values are around −8 mm.

Table 5.3 lists the predicted values of u_r^{VAUG} at the locations of the IGS GPS stations. At most stations, the radial displacement is between −5 and −6 mm. The magnitude of u_r^{VAUG} is smaller at `OHIG` (−2.3 mm), which is located at the tip of the Antarctic Peninsula, and larger at `CAS1` (−7.4 mm) and `VESL` (−6.8 mm). Station `CAS1` is located in the coastal region of Wilkes Land, where load model VAUG features broad and large ice-thickness changes. Station `VESL` is situated in Dronning Maud Land, where VAUG shows a narrow accumulation maximum.

VUNF

Load model VUNF produces magnitudes of radial displacement that exceed −4 mm over most of the Antarctic continent and reach −8 mm close to Vostok Station. For most of the Antarctic Peninsula, the values range between −2 and −5 mm.

At the IGS GPS stations, load model VUNF causes values of u_r comparable to those for VAUG (Table 5.3). The predictions are close to −4 mm, an exception being `OHIG` at the tip of the Antarctic Peninsula with −1.6 mm. The largest differences between the predictions for load models VUNF and VAUG occur at `CAS1` and `VESL`, which is mainly due to the spatial details incorporated in load model VAUG.

DOI: 10.2312/GFZ.b103-05011

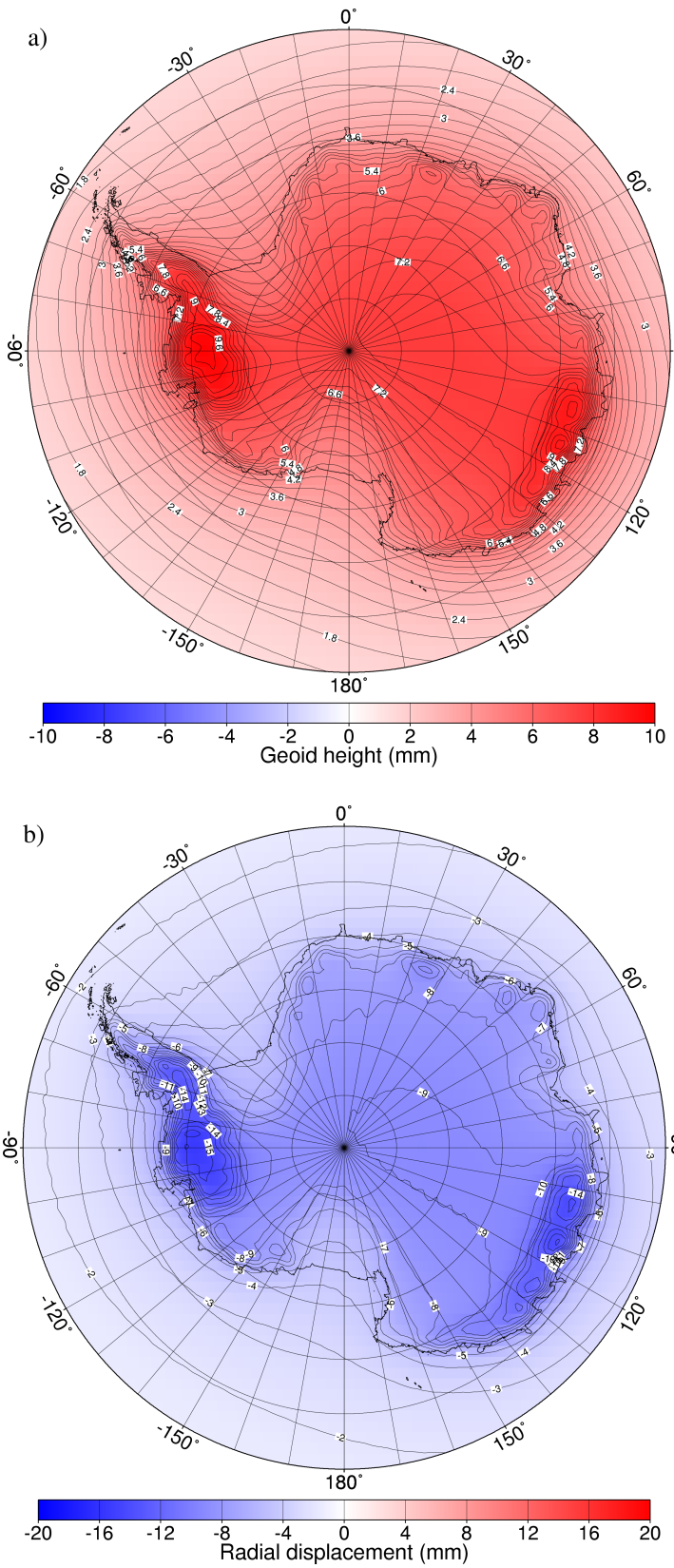

Figure 5.2: Isolines of (a) e_{G} and (b) u_r for the seasonal load model VAUG and the elastic-compressible earth model. The cut-off degree is $j_{\max} = 256$.

DOI: 10.2312/GFZ.b103-05011

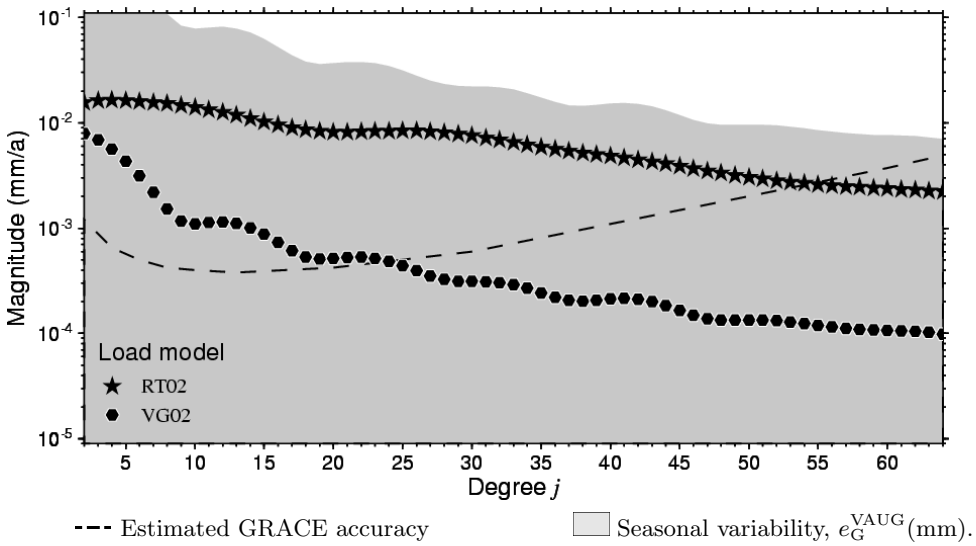

Figure 5.3: Degree-power spectrum of $\dot{e}_G$ for the secular load models RT02 and VG02 and the elastic-compressible earth model.

5.2 Secular ice-mass balance

In this section, the predictions of the elastic-compressible earth response to the secular ice-mass changes are presented. The response features monotonous changes occurring on the time scale of decades to centuries. It is expressed as rates of geoid-height change, $\dot{e}_G$, and rates of radial displacement, $\dot{u}_r$. Sections 5.2.1 and 5.2.3 address the rates of spectral and spatial geoid-height changes, respectively. The rate of radial displacement is considered in Section 5.2.3.

5.2.1 Spectral geoid-height change

RT02

The degree-power spectrum of $\dot{e}_G$ produced by the secular load model RT02 is shown in Figure 5.3. It is characterized by nearly constant power of $\sim 10^{-2}$ mm/a over the range of degrees relevant to the GRACE mission. The magnitude decreases only moderately from 2×10^{-2} mm/a for degree 2 to 2×10^{-3} mm/a for degree 64. The spectrum reflects the large variation of $<\dot{s}^I>$ over the small spatial scale observed for West Antarctica. It is expected that future estimates of the mass balance will include small-scale variations and, hence, increase the power for the high degrees in the spectrum.

VG02

The spectral signature of $\dot{e}_G$ caused by load model VG02 resembles the signature produced by VAUG (Figure 5.1), to which it is proportional by a factor of $-0.014\,a^{-1}$ (Section 4.2.2). The magnitude decreases abruptly from 8×10^{-3} mm/a for degree 2 (maximum) to 1×10^{-4} mm/a for degree 64, dropping below the estimated GRACE accuracy at degree 24. Compared to the values of $\dot{e}_G$ obtained for load model RT02, the magnitudes are strongly reduced. As both models involve the same total ice-mass

DOI: 10.2312/GFZ.b103-05011

change, this is because RT02 includes positive and negative values of $<\dot{s}^{\mathrm{I}}>$, which contribute individually to the power of the signal.

5.2.2 Spatial geoid-height change

RT02

The spatial pattern of $\dot{e}_{\mathrm{G}}$ for load model RT02 (Figure 5.4) is dominated by rates of several mm in the costal regions of West Antarctica on a small scale (~ 100 km). The highest negative rate of -3.8 mm/a is caused by the joint mass loss of the glaciers Kohler (KOH), Smith (SMI) and Thwaites (THW), which amounts to 0.11 mm/a ESL. Furthermore, two high negative rates of -2.7 mm/a and -1.8 mm/a are associated with the thinning of the glaciers DeVicq (DVQ) and Land (LAN) at rates of -875 mm/a and -547 mm/a, respectively. The largest positive rate of 0.7 mm/a is also found in West Antarctica and associated with the thickening of Ice Stream C (C) at 143 mm/a. Values of $\dot{e}_{\mathrm{G}}$ for East Antarctica are generally below 0.5 mm/a and vary on a broader scale (~ 500 km).

VG02

The spatial pattern of $\dot{e}_{\mathrm{G}}$ for load model VG02 is identical to that obtained for the seasonal load model VAUG scaled by a factor of $-0.014\,\mathrm{a}^{-1}$. The extreme values for VAUG shown in Figure 5.2, therefore, correspond to those for VG02: -0.13 mm/a over the Antarctic Peninsula, Ellsworth Land and Wilkes Land and -0.05 mm/a over central and East Antarctica.

5.2.3 Radial displacement

RT02

For load model RT02, the predictions of $\dot{u}_r$ are between -1.7 and 9.4 mm/a (Figure 5.4 b). The highest positive rates are caused by the earth's adjustment to the mass loss of the West Antarctic glaciers, the maximum negative rate is associated with the mass gain of Ice stream C. For East Antarctica, the rates are generally negative, with magnitudes of less than 0.5 mm/a. Table 5.3 lists the predicted values of $\dot{u}_r$ at the IGS GPS stations. The magnitudes are below 0.1 mm/a and, therefore, insignificant.

VG02

Load model VG02 produces very small values of $\dot{u}_r$ throughout Antarctica. As expected, the largest rates occur in the coastal regions, but are lower than 0.2 mm/a. The predictions of $\dot{u}_r$ at the IGS GPS stations (Table 5.3) are slightly higher than those for load model RT02. However, with values of ~ 0.1 mm/a, they are still insignificant.

DOI: 10.2312/GFZ.b103-05011

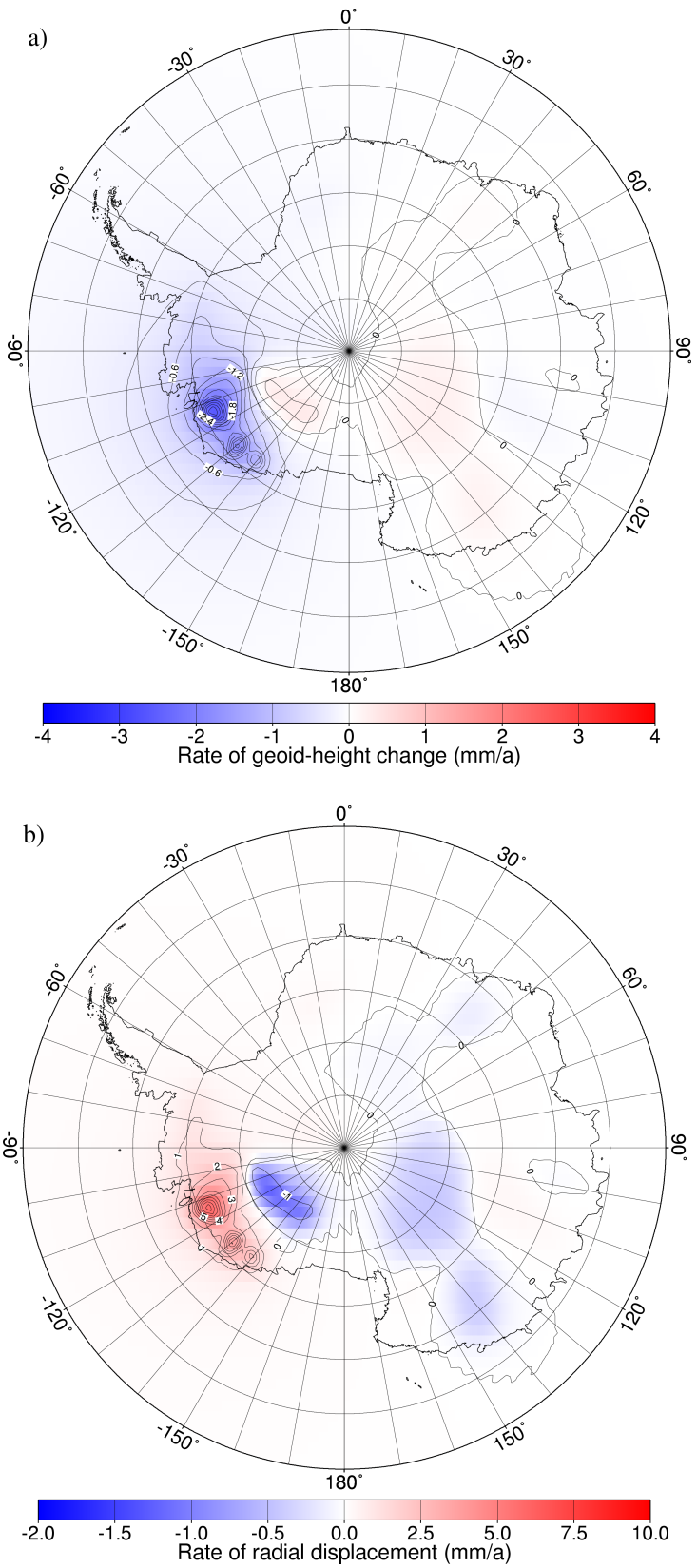

Figure 5.4: Isolines of (a) $\dot{e}_{\mathrm{G}}$ and (b) $\dot{u}_r$ for the secular load model RT02 and the elastic-compressible earth model. The cut-off degree is $j_{\max} = 256$.

DOI: 10.2312/GFZ.b103-05011

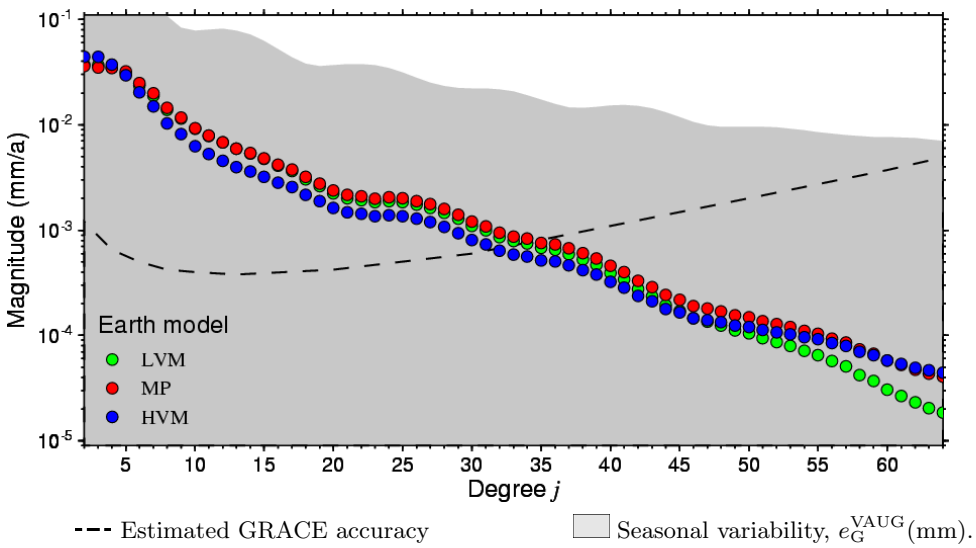

Figure 5.5: Degree-power spectrum of $\dot{e}_G$ for the Pleistocene load model ICE-3G-A and the viscoelastic-incompressible earth models LVM, MP and HVM.

5.3 Pleistocene deglaciation

This section presents the predictions of the present-day response for the viscoelastic-incompressible earth due to the deglaciation of Antarctica since the LGM. Both load models, ICE-3G-A and HUY, only consider past ice-mass changes and hence, the predicted earth response is completely PGR induced. The results as Rates of spectral and spatial geoid-height change are presented in 5.3.1 and 5.3.2, respectively, Section 5.3.3 addresses rates of radial displacement. For each deglaciation model, the calculations are performed for earth models LVM, MP and HVM.

5.3.1 Spectral geoid-height change

ICE-3G-A

The spectrum of $\dot{e}_G$ for load model ICE-3G-A shown in Figure 5.5 exhibits a signature with abruptly decreasing power towards higher degrees. This is typical of PGR-induced changes of the geoid height and caused by the low-pass filtering of the lithosphere as well as the faster relaxation of modes for higher degrees (Wu & Peltier, 1982; Wolf, 1984, 1985b).

The signature of $\dot{e}_G$ is largely independent of the underlying viscoelastic earth model. The magnitude has a maximum for degree 2, decreases by roughly one order of magnitude every 20 degrees and falls below the estimated GRACE accuracy of $\sim 10^{-3}$ mm/a near degree 33. The differences between the magnitudes for earth models LVM and MP are small. However, employing the high-viscosity model HVM causes the magnitudes of coefficients with degrees greater than 7 to decrease by 20 to 30 %, whereas those of degrees 2, 3 and 4 increase by 10 to 20 % .

DOI: 10.2312/GFZ.b103-05011

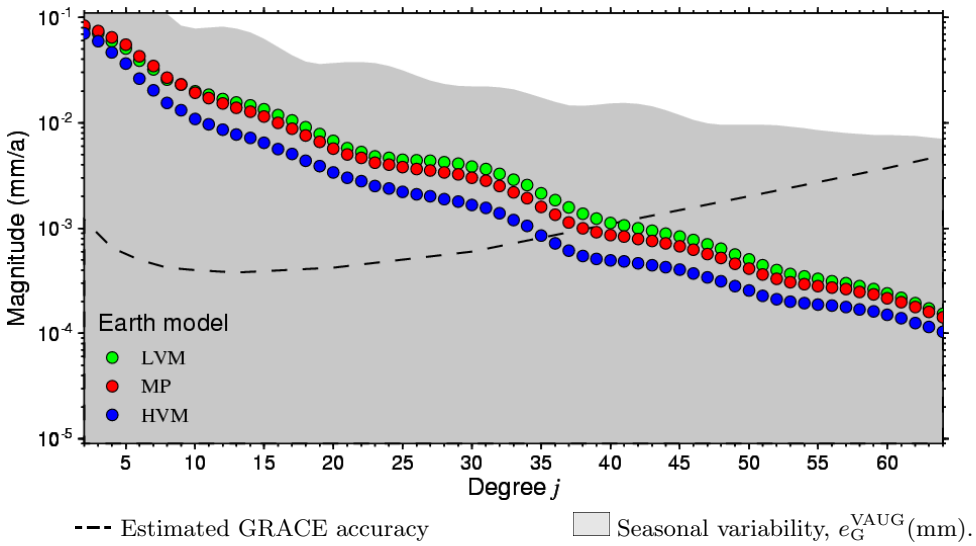

Figure 5.6: Degree-power spectrum of $\dot{e}_G$ for the Pleistocene load model HUY and the viscoelastic-incompressible earth models LVM, MP and HVM.

HUY

The spectral signature of $\dot{e}_G$ for load model HUY (Figure 5.6) is similar to that for ICE-3G-A. However, the magnitudes are 2 to 3 times larger and fall off more gradually with increasing degree. This reflects that load model HUY simulates a deglaciation which continues until today. The signature is largely independent of the earth model and similar magnitudes are obtained for LVM and MP. Employing the high-viscosity model HVM reduces the magnitudes for degrees higher than 9 by 35 to 65 %. The magnitudes for degrees below 9 are reduced significantly less. The magnitudes fall below the estimated GRACE accuracy of $\sim 10^{-3}$ mm/a near degrees 42 (LVM), 39 (MP) and 36 (HVM).

5.3.2 Spatial geoid-height change

ICE-3G-A

The spatial pattern of $\dot{e}_G$ for load model ICE-3G-A and earth model LVM is shown in Figure 5.7 a. Most of Antarctica shows positive rates, with the maximum of 0.63 mm/a located in the vicinity of the Ross Ice Shelf (215 °E, 83 °S). The Ross and Ronne Ice Shelves are surrounded by the 0.3 mm/a isoline. Over the Antarctic Peninsula and most of East Antarctica, the values of $\dot{e}_G$ range between 0.2 and 0.3 mm/a. Over the Amery Ice Shelf, the rates are ~ 0.1 mm/a.

As expected from the spectrum of $\dot{e}_G$ (Figure 5.5), the application of earth models MP and HVM retains the general spatial pattern of $\dot{e}_G$. Differences are that the medium- and high-viscosity models, MP and HVM, develop a more pronounced local maximum over the Ronne Ice Shelf and extend the area encompassed by the zero isoline.

Table 5.1 summarizes the maximum values of $\dot{e}_G$ for earth models LVM, MP and HVM over the Amery, Ross and Ronne Ice Shelves.

DOI: 10.2312/GFZ.b103-05011

HUY

The values of $\dot{e}_G$ for load model HUY are 2 to 3 times larger than those for ICE-3G-A. However, the spatial pattern, shown in Figure 5.8 a for earth model LVM, exhibits strong similarities. Most of Antarctica is surrounded by the zero isoline. The maximum rate of 1.82 mm/a occurs over the Ronne Ice Shelf (293 °E, 81 °S). Along the Antarctic Peninsula, the values of $\dot{e}_G$ are ~ 0.6 mm/a.

Table 5.1 lists the maximum values of $\dot{e}_G$ for earth models LVM, MP and HVM over the Amery, Ross and the Ronne Ice Shelves. The predictions for load models HUY and ICE-3G-A differ for the ice shelves. In the region of the Ronne Ice Shelf, the late deglaciation simulated by HUY produces larger values than over the Ross Ice Shelf, where the ice retreats earlier. In contrast to this, maximum values of $\dot{e}_G$ for ICE-3G-A are found over the Ross Ice Shelf. Moreover, HUY produces significantly larger rates over the Amery and Larsen Ice Shelves, which can mostly be attributed to the additional ice present there at the LGM.

5.3.3 Radial displacement

ICE-3G-A

Independent of the underlying earth model, load model ICE-3G-A produces the largest positive values of $\dot{u}_r$ in the regions of the Ross, Ronne and Larsen Ice Shelves. Figure 5.7 b shows isolines of $\dot{u}_r$ for the low-viscosity earth model LVM. Appreciable values are also predicted for the Amery Ice Shelf, close to Casey Station (`CAS1`, Wilkes Land) and north of George V Land. The largest negative values of $\dot{u}_r$ are roughly one order of magnitude lower. They occur offshore, close to the former ice margin, in the Amundsen, Ross and Weddel Seas and are due to the collapse of the viscoelastic forebulge.

Whereas the predicted rates for earth models LVM and MP are similar, those for HVM are reduced by 10 to 15 %. Table 5.2 summarizes the maximum values of $\dot{u}_r$ for the earth models employed and the five regions exhibiting local maxima.

HUY

The spatial pattern of $\dot{u}_r$ for load model HUY closely resembles that obtained for ICE-3G-A: maximum positive rates occur in the region of the Ronne, Ross, Larsen and Amery Ice Shelves and north of George V Land. However, compared to load model ICE-3G-A, the rates are 2 to 4 times larger. Over the Ronne Ice Shelf, the values of $\dot{u}_r$ are higher than those over the Ross Ice Shelf, where the grounded ice retreats earlier.

Table 5.2 summarizes the maximum values of $\dot{u}_r$ for the earth models employed.

DOI: 10.2312/GFZ.b103-05011

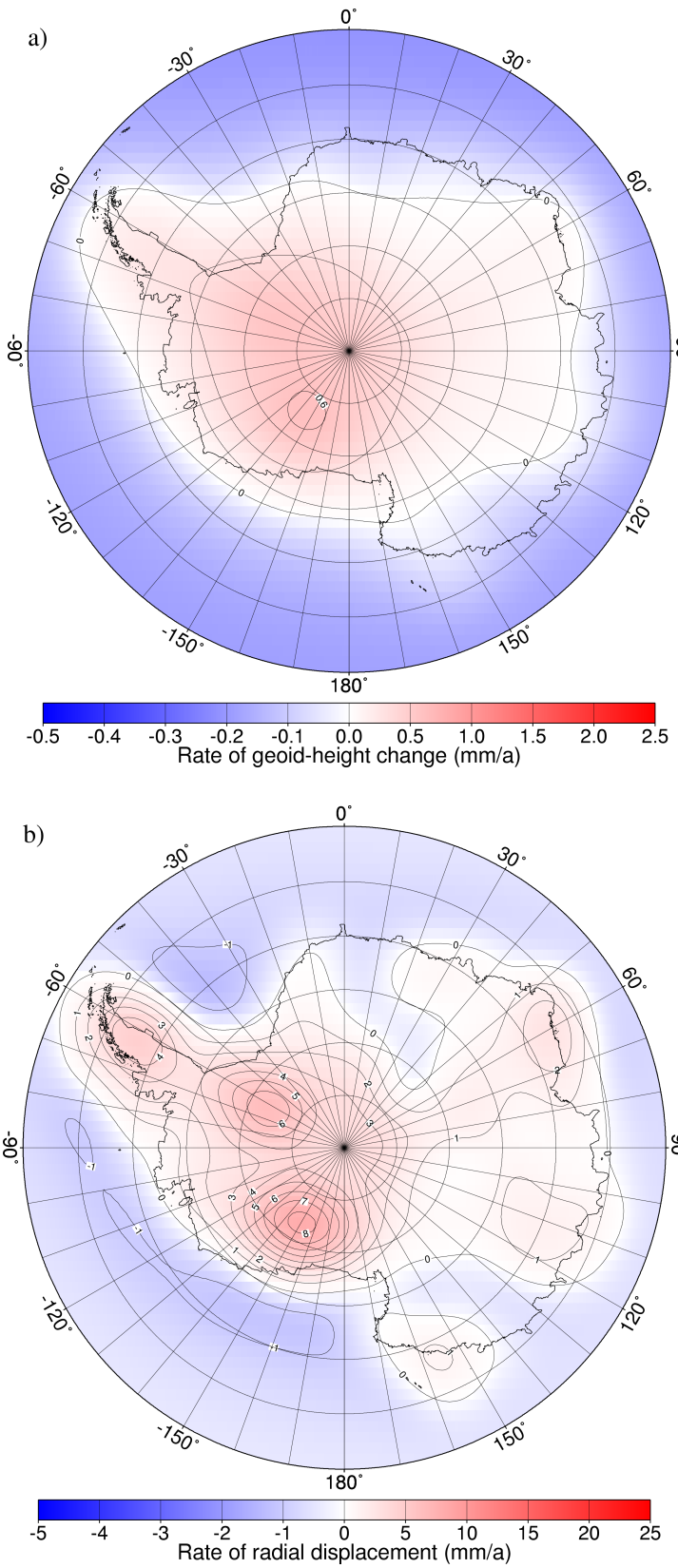

Figure 5.7: Isolines of (a) $\dot{e}_{\mathrm{G}}$ and (b) $\dot{u}_r$ for the Pleistocene load model ICE-3G-A and the viscoelastic-incompressible earth model LVM. The cut-off degree is $j_{\max} = 256$.

DOI: 10.2312/GFZ.b103-05011

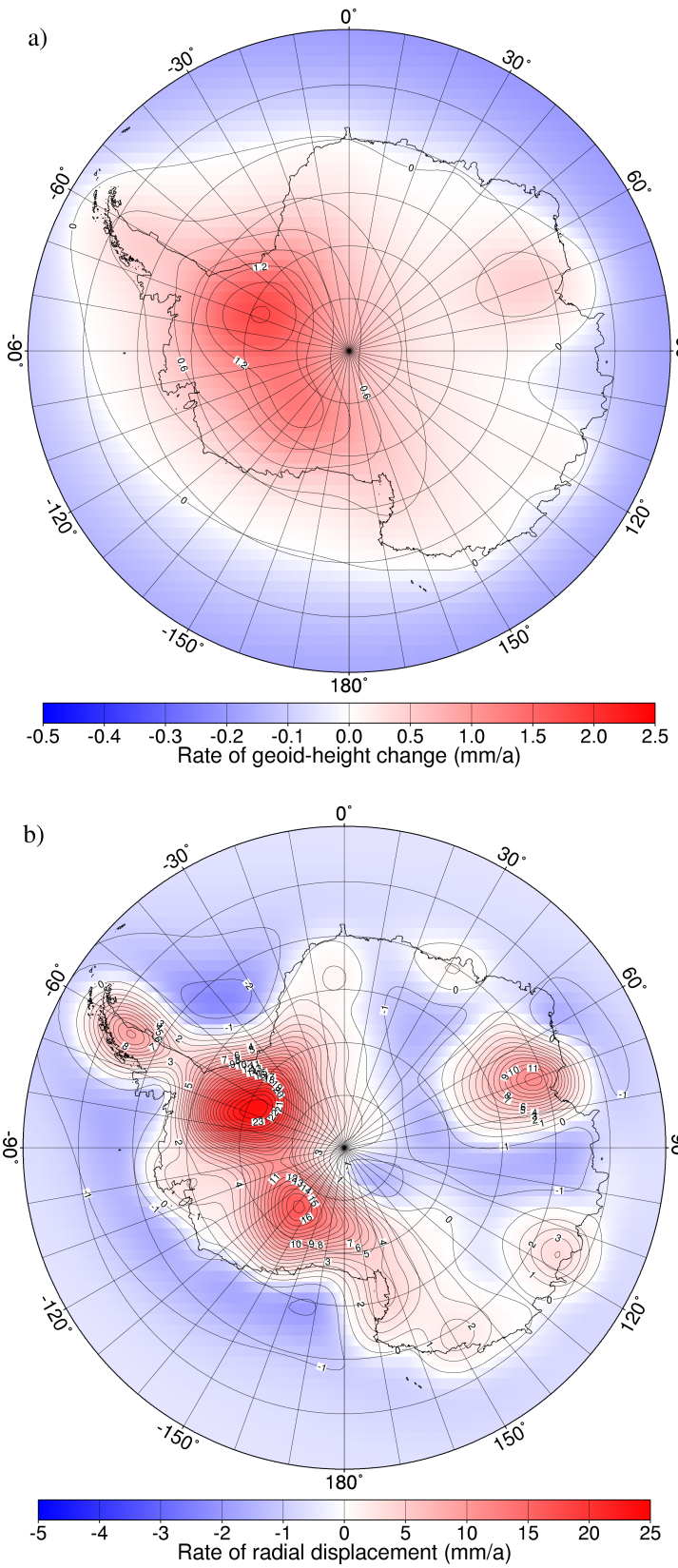

Figure 5.8: Isolines of (a) $\dot{e}_{\mathrm{G}}$ and (b) $\dot{u}_r$ for the Pleistocene load model HUY and the viscoelastic-incompressible earth model LVM. The cut-off degree is $j_{\max} = 256$.

DOI: 10.2312/GFZ.b103-05011

Table 5.1: Predictions of $\dot{e}_{\mathrm{G}}^{\max}$ for the Pleistocene load models ICE-3G-A and HUY and the viscoelastic-incompressible earth models LVM, MP and HVM. Locations of $\dot{e}_{\mathrm{G}}^{\max}$ (ICE-3G-A; HUY): Amery Ice Shelf (70 °E, 80 °S; 69 °E, 72 °S), Ross Ice Shelf (214 °E, 83 °S; 260 °E, 84 °S) and Ronne Ice Shelf (294 °E, 80 °S; 293 °E, 80 °S).

Region	$\dot{e}_{\mathrm{G}}^{\max}$ (mm/a)					
	ICE-3G-A			HUY		
	LVM	MP	HVM	LVM	MP	HVM
Amery Ice Shelf	0.18	0.20	0.29	0.49	0.40	0.29
Ross Ice Shelf	0.63	0.65	0.62	1.38	1.35	0.92
Ronne Ice Shelf	0.54	0.56	0.55	1.80	1.72	1.13

Table 5.2: Predictions of $\dot{u}_r^{\max}$ for the Pleistocene load models ICE-3G-A and HUY and the viscoelastic-incompressible earth models LVM, MP and HVM. Locations of $\dot{u}_r^{\max}$ (ICE-3G-A; HUY): Amery Ice Shelf (61 °E, 68 °S; 70 °E, 71 °S), Wilkes Land (114 °E, 70 °S; 116 °E, 68 °S), George V Land (160 °E, 80 °S; 160 °E, 80 °S), Ross Ice Shelf (209 °E, 82 °S; 214 °E, 83 °S), Ronne Ice Shelf (298 °E, 80 °S; 292 °E, 80 °S) and Larsen Ice Shelf (298 °E, 68 °S; 298 °E, 68 °S).

Region	$\dot{u}_r^{\max}$ (mm/a)					
	ICE-3G-A			HUY		
	LVM	MP	HVM	LVM	MP	HVM
Amery Ice Shelf	2.86	3.05	2.29	12.53	9.50	5.33
Wilkes Land	1.47	1.57	1.32	4.06	3.29	2.10
George V Land	1.37	1.42	1.47	4.36	5.45	4.15
Ross Ice Shelf	8.38	8.93	6.74	17.31	15.94	9.62
Ronne Ice Shelf	6.16	6.45	4.95	24.65	21.19	12.18
Larsen Ice Shelf	4.97	5.44	4.12	10.16	7.93	4.81

DOI: 10.2312/GFZ.b103-05011

Table 5.3: Predictions of u_r and $\dot{u}_r$ at the IGS GPS stations for the seasonal load models VAUG and VUNF, the secular load models RT02 and VG02 and the elastic-compressible earth model.

		u_r (mm)		$\dot{u}_r$ (mm/a)	
ID	Station	VAUG	VUNF	RT02	VG02
SYOG	Syowa	5.65	4.08	−0.00	0.08
MAW1	Mawson	5.16	3.90	0.01	0.07
DAV1	Davis	5.36	4.06	0.01	0.08
CAS1	Casey	7.84	3.78	0.04	0.11
MCM4	Mc Murdo	5.24	4.10	0.02	0.07
OHIG	O'Higgins	2.42	1.34	0.09	0.03
VESL	Sanae IV	6.77	4.26	0.06	0.09

Table 5.4: Predictions of $\dot{u}_r$ at the IGS GPS stations for the Pleistocene load models ICE-3G-A and HUY and the viscoelastic-incompressible earth models LVM, MP and HVM.

		$\dot{u}_r$ (mm/a)					
ID	Station	ICE-3G-A			HUY		
		LVM	MP	HVM	LVM	MP	HVM
SYOG	Syowa	0.42	0.49	0.58	0.02	0.01	0.14
MAW1	Mawson	2.76	2.98	2.26	−0.10	0.20	0.18
DAV1	Davis	1.09	1.14	1.00	3.43	2.89	1.70
CAS1	Casey	1.03	1.03	0.81	1.48	1.29	0.91
MCM4	Mc Murdo	0.38	0.36	0.69	3.98	5.13	4.00
OHIG	O'Higgins	1.65	1.71	1.30	1.76	1.34	0.93
VESL	Sanae IV	−0.26	−0.15	0.20	0.56	0.49	0.53

DOI: 10.2312/GFZ.b103-05011

6

Discussion

In this chapter, the predictions of the geoid-height change and the radial displacement are compared with the observations. For this purpose, the results obtained for the different time scales of the AIS's evolution are superimposed.

Section 6.1 addresses the spectral and spatial geoid-height changes, where the comparison with the GRACE observations is carried out for three time intervals. Section 6.2 discusses the rates of radial displacement at the IGS-maintained Antarctic GPS stations. Additionally, predictions are presented for two GPS transects in East and West Antarctica.

6.1 Comparison with GRACE observations

For the following comparison of predicted geoid-height changes, e_{G}, with GRACE observations, three time intervals are considered: (a) August 2002 to August 2003, (b) August 2002 to November 2002 and (c) April 2003 to May 2003. These time intervals are chosen with regard to the predicted seasonal geoid-height change, which is zero for interval (a), large and negative for interval (b) and large and positive for interval (c). The predictions superimpose the results for the load models considered as most realistic: the seasonal load model VAUG, the secular load model RT02 and the Pleistocene load model HUY.

A conservative estimate of the cut-off degree for the present spectral GRACE resolution is $j_{\max} = 13$, which corresponds to a half wavelength of $\sim 1500\,\mathrm{km}$ at the earth's surface. As a consequence, coefficients of higher degree and order are ignored for the predictions. Moreover, for this preliminary comparison, coefficients of degree and order lower than 3 are also neglected.

In the following, the GRACE data for the global geoid-height change are confined to the region of Antarctica by neglecting any data north of 60 °S. Then, a spherical-harmonic expansion up to degree $j_{\max} = 340$ is performed and degree-power coefficients are calculated. In the degree-power spectra for GRACE (Figure 6.1), only those degrees and orders present in the initial spatial data set ($j, m = 3, ..., 13$) are considered.

It is not completely justified to neglect the degrees and orders 0, 1 and 2, which describe, respectively, the principle of mass conservation, the origin of the coordinate system and, to a large part, the mass exchange between the hemispheres. However, including these contributions would require the extension of the regional investigation to the entire globe. Moreover, the coordinate system of the computational model would have to be transformed to the system underlying the satellite observations,

DOI: 10.2312/GFZ.b103-05011

which is not completely solved yet.

Section 6.1.1 discusses the degree-power spectra of e_G for the predictions and the observations. Section 6.1.2 compares the corresponding spatial patterns of e_G.

6.1.1 Spectral geoid-height change

The degree-power spectra of the predicted and observed values of e_G for the interval August 2002 to August 2003 are shown in Figure 6.1 a. Over the range of degrees available from GRACE, the prediction is dominated by the PGR-induced geoid-height change evident as a pronounced decrease of the magnitude with increasing degree from 7×10^{-2} mm for degree 3 to 1×10^{-2} mm for degree 13. The signature of the GRACE observation does not share this characteristic. The magnitudes are larger ($\sim 10^{-1}$ mm) and nearly constant.

The spectrum of e_G for the interval between August 2002 and November 2002 (Figure 6.1 b) is dominated by the seasonal geoid-height change. The degree power for the prediction exceeds 10^{-1} mm, but not pronounced in the GRACE signature. In particular, the predicted and observed values of e_G differ for degrees smaller than 7.

For the interval April 2003 to May 2003 (Figure 6.1 c), the predictions essentially reflect the seasonal geoid-height change, although with less power. For this interval, the predicted and observed signatures agree best. Overall, the GRACE spectra for the three time intervals considered are very similar and do not correspond to the predicted seasonal variations.

6.1.2 Spatial geoid-height change

The spatial pattern of e_G for the predictions and the observations for the three time intervals considered is shown in Figure 6.2. The sign of the geoid-height change is defined by $e_G(t_{later}) - e_G(t_{earlier})$.

At the cut-off degree $j_{max} = 13$, the prediction of $\dot{e}_G$ for the annual time interval, here August 2002 to August 2003, shows a positive anomaly over the shelf areas with ongoing PGR and a negative anomaly over the rapidly thinning glaciers along the Antarctic west coast. In contrast to this, the GRACE observations show a multitude of stronger positive and negative anomalies of $\dot{e}_G$ with centres located offshore (Figure 6.2 a). During the time interval August 2002 to November 2002, the predictions show a seasonal decrease of the geoid height of several mm not reflected in the GRACE observations (Figure 6.2 b). The strong increase of the geoid height predicted between April 2003 and May 2003 is also not present in the data (Figure 6.2 c).

Taken together, the predicted and GRACE-observed geoid-height changes do not correspond yet. Independent of the time interval chosen, the observations exhibit several strong anomalies surrounding the Antarctic continent not explained by the glacial changes modelled.

It is suggested that these anomalies are due to mass redistributions associated with ocean tides, which have not been successfully removed from the GRACE data yet (Schmidt, *pers. comm.*, GFZ Potsdam, 2004). The predictions of the employed ocean-tide model, FES-2002 (e.g. Lefèvre *et al.*, 2000), are most accurate for areas where satellite-altimetry data exist. In this model, shortcomings for high latitudes and coastal regions, in particular for the oceans surrounding Antarctica, are present.

An appraisal of the GRACE-observed geoid-height change due to mass changes in the oceans is obtained by considering the difference between the changes during two

DOI: 10.2312/GFZ.b103-05011

annual time intervals, here from August 2002 to August 2003 and from May 2002 to May 2003 (Figure 6.3). Compared to the three time intervals considered, this difference exhibits a similar spatial pattern, with magnitudes on the order of several mm. However, the peak magnitudes are now located offshore. Over the Antarctic continent, the magnitudes are $\sim 1\,\mathrm{mm}$ and small compared to those caused by the seasonal ice-mass variations. It is an unsolved problem why not even the sign of the predicted seasonal geoid-height change is present in the GRACE data. One possibility is that seasonal hydrological variations on the northern hemisphere induce a shift of the geoid height over Antarctica. This problem can possibly be solved by extending the modelling to the entire globe and by using coordinates consistent with those employed in satellite geodesy.

DOI: 10.2312/GFZ.b103-05011

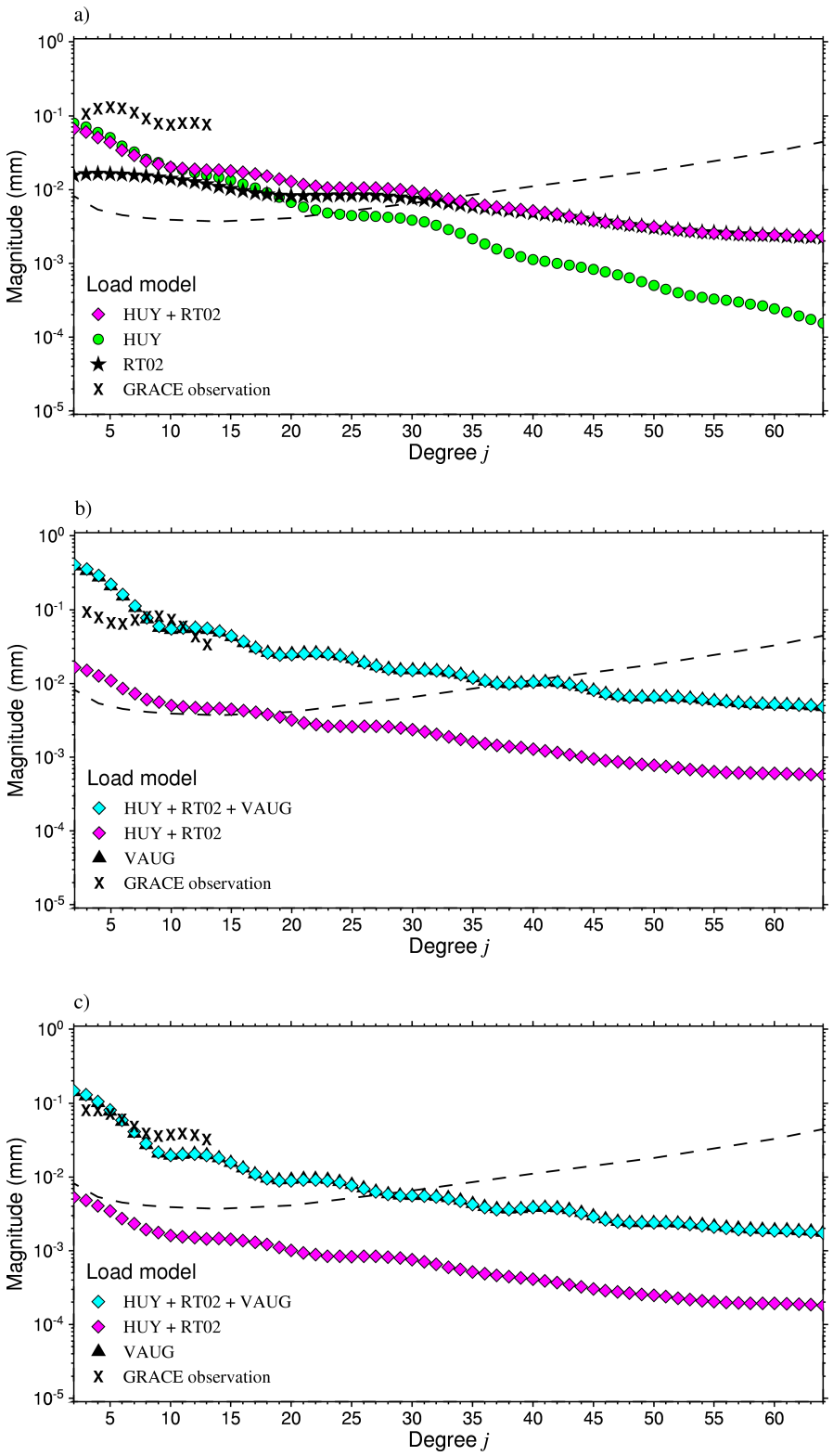

Figure 6.1: Degree-power spectrum of e_G for predictions and GRACE observations. (a) August 2002 to August 2003, (b) August 2002 to November 2002 and (c) April 2003 to May 2003.

DOI: 10.2312/GFZ.b103-05011

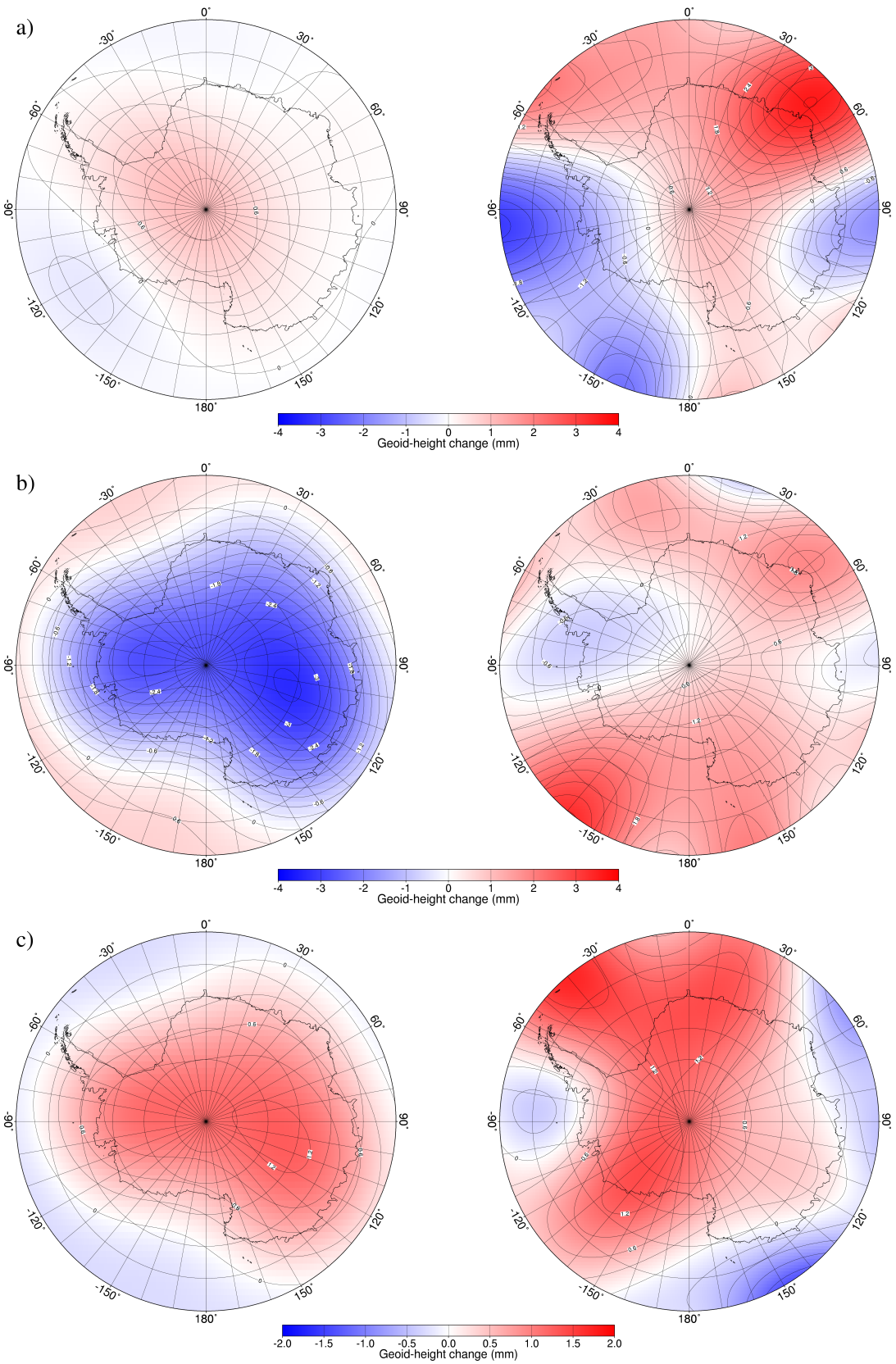

Figure 6.2: Isolines of e_G for predictions (left) and GRACE observations (right). (a) August 2002 to August 2003, (b) August 2002 to Novemmber 2002 and (c) April 2003 to May 2003. The cut-off degrees are $j_{min} = 3$ and $j_{max} = 13$.

DOI: 10.2312/GFZ.b103-05011

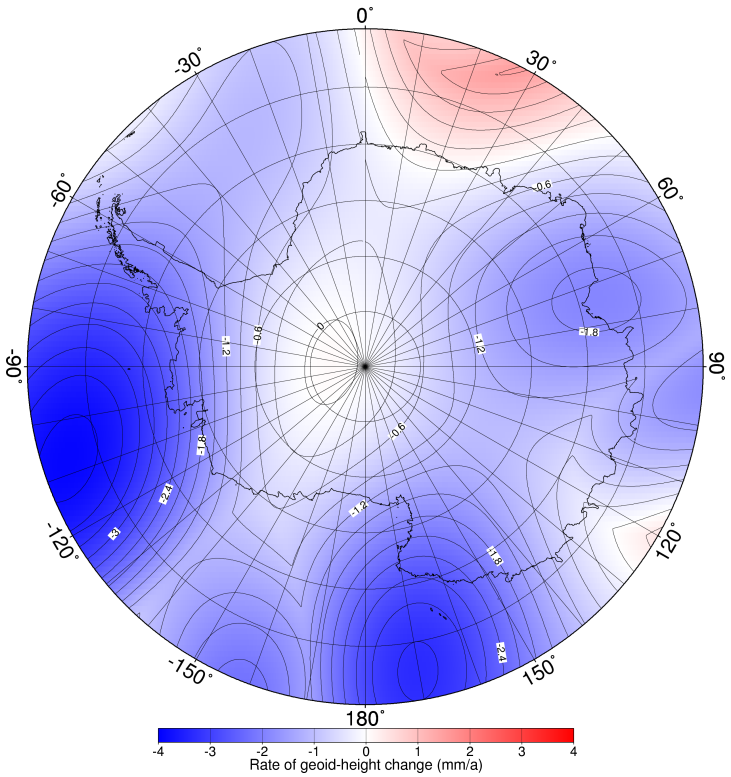

Figure 6.3: Isolines of e_{G} for the difference between two annual GRACE observations. May 2002 to May 2003 minus August 2002 to August 2003. The cut-off degrees are $j_{\min} = 3$ and $j_{\max} = 13$.

DOI: 10.2312/GFZ.b103-05011

6.2 Comparison with GPS observations

This section considers rates of land uplift at existing and potential GPS sites in Antarctica. Section 6.2.1 compares predicted and observed rates at the IGS GPS stations and discusses whether their locations are suitable for determining GIA-induced uplift. The observed uplift rates are provided by the International GPS Service (2003 *[online]*). Section 6.2.2 provides predictions along transects A–A′ and B–B′ and discusses which transect (or part of it) is most sensitive to which aspect of the changes of the AIS.

6.2.1 IGS-operated GPS stations

Figure 6.4 displays predicted rates of land uplift, $\dot{u}_r$, for the earth and load models employed (except for the seasonal load model VUNF) for the locations of the IGS GPS stations. The estimated uplift rates, $\dot{u}_r^{\mathrm{obs}}$, based on linear-trend analyses of the IGS solutions, are indicated as dotted horizontal lines, the predicted seasonal variability, u_r^{VAUG}, as grey-shaded areas. Table 6.1 lists the minimum and maximum predictions of $\dot{u}_r$ for a combination of secular and Pleistocene load models as well as the seasonal variability, u_r^{VAUG}, and the IGS GPS observations, $\dot{u}_r^{\mathrm{obs}}$.

Obviously, only PGR-induced uplift rates are significant. The predictions of $\dot{u}_r$ for the secular ice-mass balances, RT02 and VG02, are below 0.2 mm/a and therefore negligible. However, the predicted rates tend to be lower than the observations, exceptions being Mc Murdo (`MCM4`), Davis (`DAV1`) and Mawson (`MAW1`) where the PGR-induced predictions are either much higher or close the observations. The seasonal variability, u_r^{VAUG}, ranges between 2 and 8 mm, which is on the order of the annual signal recorded by GPS stations and exemplifies the necessity of using long time series for estimating the secular uplift trend.

Figure 6.4 also shows that the values of $\dot{u}_r$ are most sensitive to the deglaciation history, whereas the underlying earth model is of secondary importance. However, the predictions for load model HUY are not systematically higher than those for ICE-3G-A, as might be expected from the maximum uplift rates listed in Table 5.2. For instance, in the region of the Amery Ice Shelf, load model ICE-3G-A differs from HUY by featuring the largest ice masses closer to Mawson (`MAW1`), which increases the uplift rates at this GPS station. At Mc Murdo (`MCM4`), the situation is opposite. It is concluded that the PGR-induced uplift rates at the GPS stations do not represent the bulk characteristics of the deglaciation history, but are mainly influenced by the regional details of the ice retreat, which are difficult to constrain.

It is questionable if the earth and load models used are adequate to calculate the earth's response at the locations of the GPS receivers. This is because all stations are situated close to the transition from a continental to an oceanic rheology, which is not described by the radially symmetric earth model employed. Gasperini *et al.* (1990) and others showed that lateral variations of the lithosphere thickness produce a distinctly different response along the rheological transition (see Martinec & Wolf, 2004, for a review).

Moreover, all GPS sites are also close to the viscoelastic forebulge. Its development is very sensitive to the underlying rheology and the spatial distribution and migration of the ice load (e.g. Milne, 1998). As mentioned above, the deglaciation histories are particularly questionable near the ice sheet margin. Another problem may be that, in this study, melt water from the retreating ice sheet is uniformly distributed over

DOI: 10.2312/GFZ.b103-05011

the present ocean such that its area remains constant as the grounding line of the ice sheet retreats. This neglects that the water is redistributed according to the changes of the geoid height and the radial displacement, which may influence the predicted uplift rates particularly at the migrating transition between ice and ocean.

Another problem is that the measurements at most GPS stations probably contain a tectonic component. In particular, at Mc Murdo (MCM4), which is located near the Transantarctic Mountains, the observed uplift rates may be strongly influenced by non-isostatic contributions (e.g. Raymond *et al.*, 2000).

Table 6.1: Predictions of $\dot{u}_r$ at the IGS GPS stations for combinations of the Pleistocene load models ICE-3G-A and HUY with the secular load models RT02 and VG02. The values incorporate the minimum and maximum PGR-induced uplift rates considering the earth models employed (LVM, MP and HVM) and averaged rates associated with the secular load models RT02 and VG02. Also shown are the predictions of u_r for the seasonal load model VAUG and the observations $\dot{u}_r^{\mathrm{obs}}$.

		$\dot{u}_r$ (mm/a)				u_r (mm)	$\dot{u}_r^{\mathrm{obs}}$ (mm/a)
		min	max	min	max		
ID	Station	ICE-3G-A + RT02 + VG02		HUY + RT02 + VG02		VAUG	IGS
SYOG	Syowa	0.46	0.62	0.05	0.18	5.65	2.10
MAW1	Mawson	2.30	3.02	−0.06	0.24	5.16	2.80
DAV1	Davis	1.04	1.18	1.74	3.47	5.36	4.20
CAS1	Casey	0.88	1.10	0.98	1.55	7.84	3.70
MCM4	Mc Murdo	0.41	0.74	4.03	5.18	5.24	0.80
OHIG	O'Higgins	1.36	1.77	0.99	1.82	2.42	9.50
VESL	Sanae IV	−0.19	0.27	0.56	0.63	6.77	−1.40

DOI: 10.2312/GFZ.b103-05011

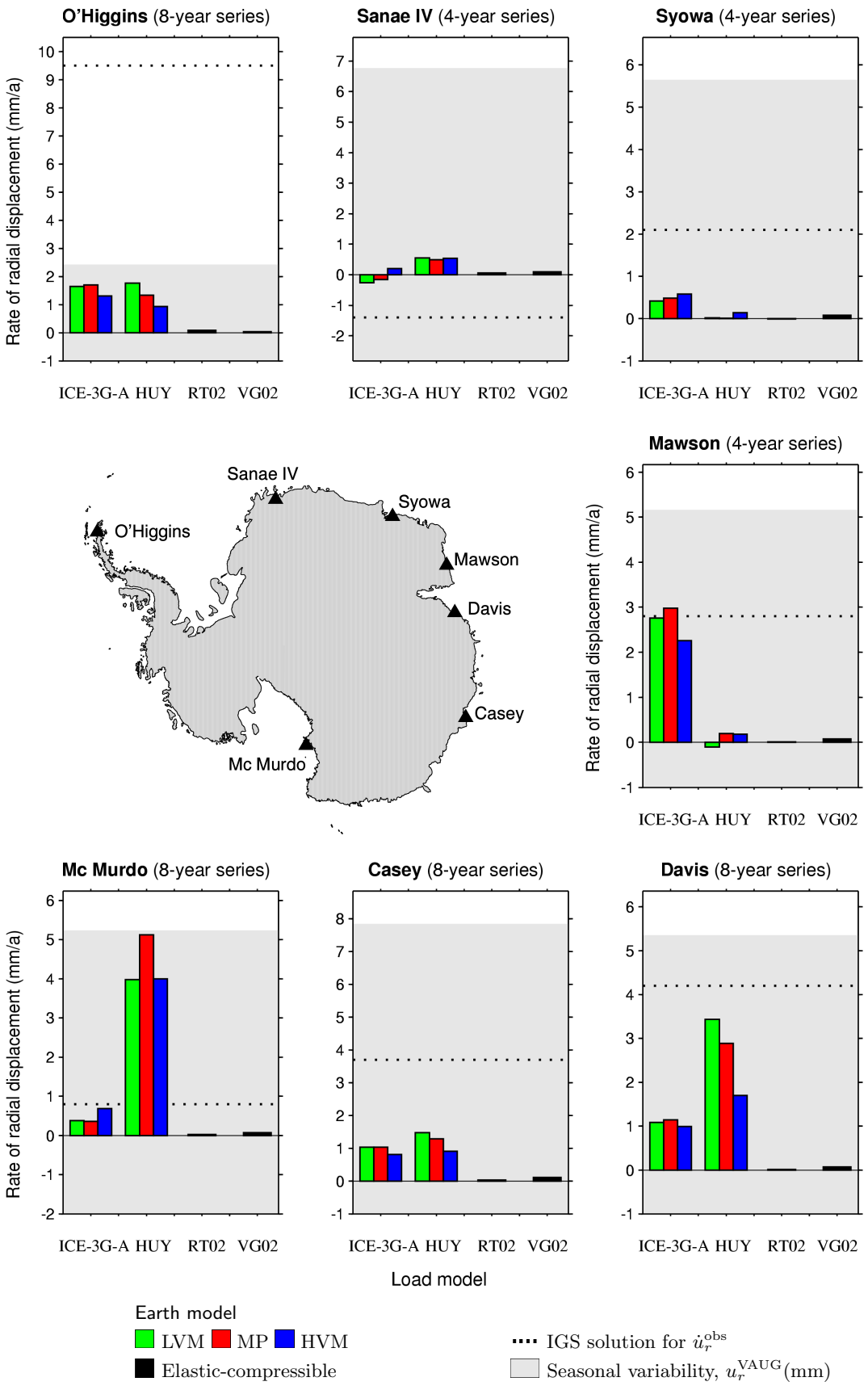

Figure 6.4: Predictions and observations of $\dot{u}_r$ for the IGS GPS stations. The GPS solutions for $\dot{u}_r^{\mathrm{obs}}$ are taken from the International GPS Service (2003 *[online]*).

DOI: 10.2312/GFZ.b103-05011

6.2.2 Transect A–A′ and transect B–B′

Figure 6.5 a and b shows rates of land uplift, $\dot{u}_r$, along transect A–A′ in the Prince Charles Mountains, East Antarctica, and along transect B–B′, stretching roughly from O'Higgins to Mc Murco Station, West Antarctica. Indicated are values of $\dot{u}_r$ associated with the three viscoelastic earth models and the Pleistocene load models ICE-3G-A and HUY. As for the locations of the IGS GPS stations, the rates produced by the secular ice-mass balances lie below 0.1 mm/a and are therefore neglected. The seasonal variability, u_r^{VAUG}, is shown as grey-shaded area.

Along transect A–A′ (Figure 6.5 a), load model HUY produces a typical PGR signature of uplift rates. The largest rate occurs at the distance 400 km of the transect, close to the centre of the Amery Ice Shelf, and amounts to 12.0, 9.0 and 5.0 mm/a for earth models LVM, MP and HVM, respectively. The rates for load model ICE-3G-A are much lower and nearly constant along the transect, ranging between 1.2 and 2.4 mm/a. This can be explained by the westward shift of ice in this region described by the load model. The seasonal variability of the land uplift is ~ 7 mm and, thus, on the order of the annual uplift due to PGR.

Transect B–B′ (Figure 6.5 b) is subdivided into three segments: B–B1 and B1–B2 crossing the Larsen and Ronne Ice Shelves, respectively, and B2–B′, being parallel to the Ross Ice Shelf.

Along segments B–B1 and B1–B2, predictions of $\dot{u}_r$ for both load models show a typical PGR signature. The largest rates are predicted for HUY along B1–B2 and amount to 24.0, 20.6 and 11.9 mm/a for earth models LVM, MP and HVM, respectively. Along B1–B2, the rates are significantly lower and amount to 8.9, 6.9 and 4.1 mm/a for LVM, MP and HVM, respectively. Along these segments, the predictions of $\dot{u}_r$ for ICE-3G-A are lower, more uniform and differ only by ~ 1 mm/a between the earth models. The largest rates are obtained for MP and amount to 5.8 and 5.2 mm/a along segments B–B1 and B1–B2, respectively.

Along segment B2–B′, the rates produced by HUY do not reflect the retreat of large ice masses in the region of the Ross Ice Shelf. The values of $\dot{u}_r$ proximal to the region of the expected maximum uplift merely range between 4 and 8 mm/a. For ICE-3G-A, the rates are lower and show a maximum of ~ 4 mm/a at the distance 3400 km of the transect.

Transect A–A′ and segments B–B1 and B1–B2 of transect B–B′ prove to be suitable for detecting PGR. Particularly, GPS observations along segments B–B1 and B1–B2 impose constraints on the deglaciation history. Although most of the transect crosses areas of shelf ice, rock outcrops exist within a distance of ~ 250 km.

The usefulness of segment B2–B′ of transect B–B′ for detecting PGR-induced uplift is questionable. The transect follows the Transantarctic Mountains, which delineate a tectonic boundary indicative of a laterally heterogenous earth. Moreover, GIA-induced uplift rates in this area are likely to be small compared to those tectonically induced.

DOI: 10.2312/GFZ.b103-05011

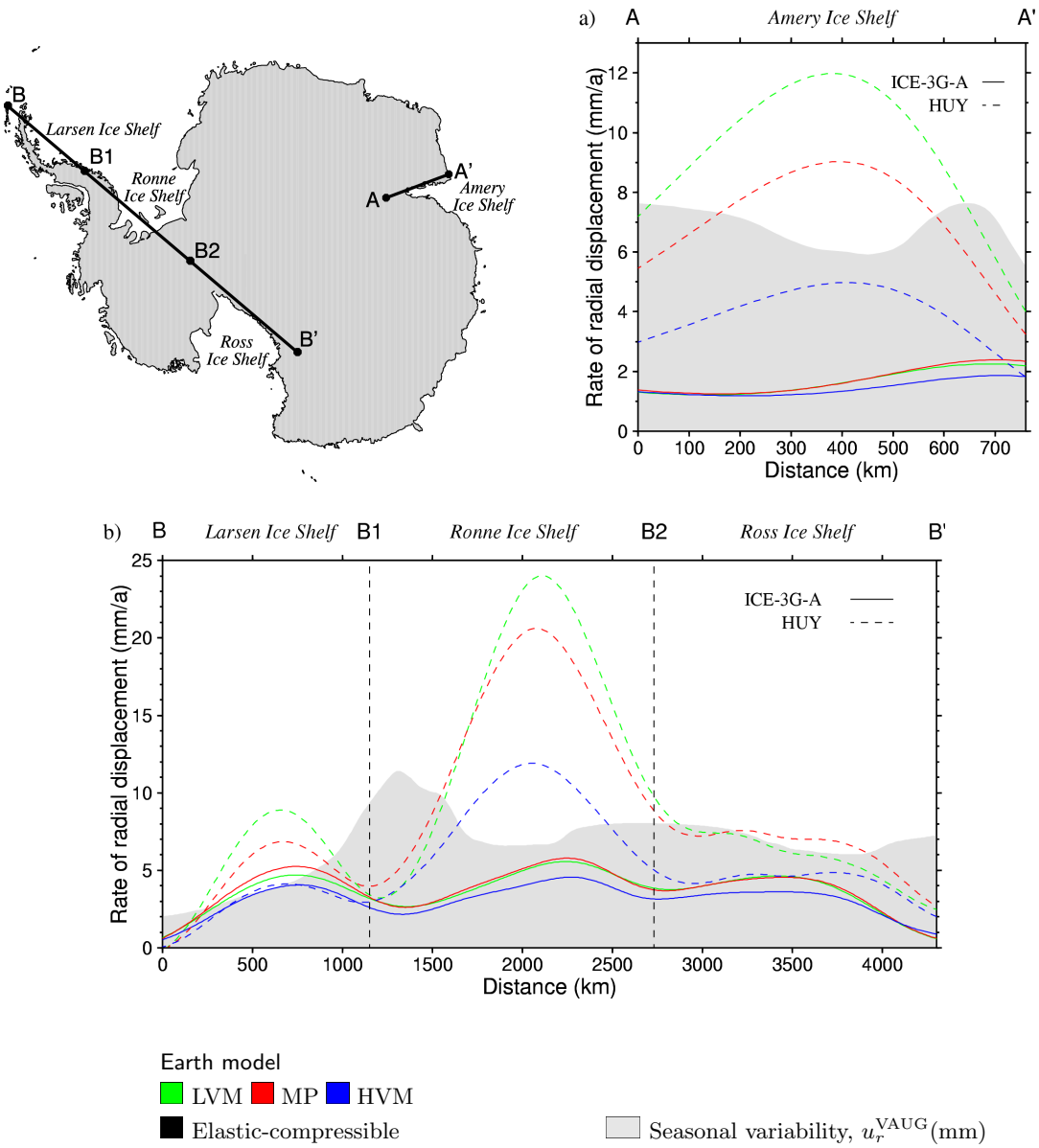

Figure 6.5: Predictions of $\dot{u}_r$ along (a) transect A–A′ (800 km, East Antarctica) and (b) transect B–B′ (4500 km, West Antarctica).

DOI: 10.2312/GFZ.b103-05011

A

Mathematical supplements

A.1 Surface spherical harmonics

A scalar field described by a square-integrable scalar function, $f(\vartheta, \varphi)$, defined on the unit sphere $\mathbf{S}^2 := [0, \pi] \times [-\pi, \pi]$ can be expanded into a series of surface spherical harmonics in the form

$$f(\vartheta, \varphi) = \sum_{j=0}^{\infty} \sum_{m=-j}^{j} F_{jm} Y_{jm}(\vartheta, \varphi), \tag{A.1}$$

where F_{jm} are the complex, fully normalized spherical-harmonic coefficients of degree j and order m, ϑ and φ are the colatitude and longitude, respectively, and $Y_{jm}(\vartheta, \varphi)$ are the surface spherical-harmonic functions given by

$$Y_{jm}(\vartheta, \varphi) = P_{jm}(\cos\vartheta) e^{\mathrm{i}m\varphi}, \tag{A.2}$$

with P_{jm} the fully normalized associated Legendre functions of degree j and order m[1]. The surface spherical harmonics, $Y_{jm}(\vartheta, \varphi)$, are complete and orthonormal on $\mathbf{S}^2$, which allows the coefficients F_{jm} to be expressed as

$$F_{jm} = \int_{-\pi}^{\pi} \int_{0}^{\pi} f(\vartheta, \varphi) Y^*_{jm}(\vartheta, \varphi) \sin\vartheta d\vartheta d\varphi, \tag{A.3}$$

where the asterisk denotes complex conjugation. In addition, if $f(\vartheta, \varphi)$ is real, it holds that

$$F_{j,-m} = (-1)^m F^*_{jm}, \tag{A.4}$$

and the zonal coefficients, F_{j0}, are also real.

In geodesy, the spherical-harmonic expansion is particularly relevant for the description of the earth's gravitational field. However, it is common to adopt the geodetic norm (e.g. Heiskanen & Moritz, 1967) rather than the quantum-mechanics norm (e.g. Varshalovich, 1989) employed in this study, and express the fields in terms of the fully normalized Stokes coefficients, $\bar{C}_{jm}$ and $\bar{S}_{jm}$, which are related to the coefficients in the quantum-mechanics norm by

$$\begin{aligned} F_{j0} &= \sqrt{4\pi}\bar{C}_{j0}, && m = 0, \\ \mathrm{Re}\, F_{jm} &= (-1)^m \sqrt{2\pi}\bar{C}_{jm}, && m > 0, \\ \mathrm{Im}\, F_{jm} &= (-1)^{m+1} \sqrt{2\pi}\bar{S}_{jm}, && m > 0. \end{aligned} \tag{A.5}$$

[1] $\sum_{j=0}^{\infty} \sum_{m=-j}^{j}$ is henceforth denoted by $\sum_{jm}$.

DOI: 10.2312/GFZ.b103-05011

The coefficients in the spherical-harmonic expansion of a function depend on the choice of the coordinate system. However, the variance of F_{jm} defined by

$$\delta F_j^2 := \frac{1}{4\pi} \sum_{m=-j}^{j} F_{jm} F_{jm}^* = \sum_{m=0}^{j} (\bar{C}_{jm}^2 + \bar{S}_{jm}^2) \tag{A.6}$$

and the degree power, $|\delta F_j|$, are quantities independent of the orientation of the coordinate system and, therefore, allow the comparison of the spectra of two scalar fields. A graph of δF_j^2 versus j is called a degree-variance spectrum, whereas a graph of $|\delta F_j|$ versus j is called a degree-power spectrum. In this study, spectra of the geoid height, e_{G}, and the rate of geoid-height change, $\dot{e}_{\mathrm{G}}$, are plotted as degree-power spectra. The geoid height, e_{G}, is calculated from the gravitational potential, ϕ, and the gravitational force at the earth's surface, $g^{(0)}(a)$, according to

$$e_{\mathrm{G}}(\mathbf{\Omega}, t) = \phi(\mathbf{\Omega}, t)/g^{(0)}(a). \tag{A.7}$$

A.2 Spatial convolution

The earth's elastic response to an arbitrary static load distribution is calculated by the spatial convolution of the appropriate Green's function with the load distribution:

$$f(\mathbf{\Omega}) = \int_{\mathbf{\Omega}'} a^2 f^{\mathrm{G}}(\mathbf{\Omega} - \mathbf{\Omega}') \sigma(\mathbf{\Omega}') d\mathbf{\Omega}', \tag{A.8}$$

where $f(\mathbf{\Omega})$ represents the radial surface displacement, u_r, or the geoid height, e_{G}, a is the radius of the earth, f^{G} the corresponding Green's function and $\mathbf{\Omega}'$ and $\mathbf{\Omega}$ are the solid angles associated with the load and the prediction, respectively. The spherical-harmonic representation of the Green's function according to

$$f^{\mathrm{G}}(\mathbf{\Omega}) = \sum_{jm} F_{jm}^{\mathrm{G}} Y_{jm}(\mathbf{\Omega}) \tag{A.9}$$

becomes independent of m for radial symmetry:

$$f^{\mathrm{G}}(\vartheta) = \sum_{j} F_{j0}^{\mathrm{G}} Y_{j0}(\vartheta). \tag{A.10}$$

With the spherical-harmonic representation of the surface-mass density according to

$$\sigma(\mathbf{\Omega}) = \sum_{jm} \sigma_{jm} Y_{jm}(\mathbf{\Omega}), \tag{A.11}$$

(A.8) takes the form

$$f(\mathbf{\Omega}) = \int_{\mathbf{\Omega}'} a^2 \sum_{j} F_{j0}^{\mathrm{G}} Y_{j0} \sum_{j'm'} \sigma_{j'm'} Y_{j'm'}(\mathbf{\Omega}') d\mathbf{\Omega}'. \tag{A.12}$$

This expression can be contracted by applying the addition theorem and the orthonormal property of the surface spherical harmonics, giving

$$f(\mathbf{\Omega}) = a^2 \sum_{j} F_{j0}^{\mathrm{G}} \sqrt{\frac{4\pi}{2j+1}} \sum_{m} \sigma_{jm} Y_{jm}(\mathbf{\Omega}), \tag{A.13}$$

DOI: 10.2312/GFZ.b103-05011

which can be written in terms of the load Love numbers, q_j^i, by

$$f^i(\mathbf{\Omega}) = a^2 \sum_j q_j^i \frac{4\pi}{2j+1} \sum_m \sigma_{jm} Y_{jm}(\mathbf{\Omega}). \tag{A.14}$$

Here, $i \in \{h, k\}$ indicates radial displacement or geoid height. In this study, $u_r(\mathbf{\Omega}) = f^h(\mathbf{\Omega})$ and $e_{\mathrm{G}}(\mathbf{\Omega}) = f^k(\mathbf{\Omega})/g^{(0)}(a)$.

DOI: 10.2312/GFZ.b103-05011

References

ADD Consortium, 2000 *[online]*. *Antarctica Digital Database, Version 3.0, Database, Manual and Bibliography*, Scientific Commitee on Antarctic Research (SCAR), Cambridge. http://www.add.scar.org/, cited: Aug. 2003.

Anderson, J. B., Shipp, S. S., Lowe, A. L., Wellner, J. S. & Mosola, A. B., 2002. The Antarctic ice sheet during the last glacial maximum and its subsequent retreat history: a review. *Quat. Sci. Rev.*, 21(1-3): 49–70.

Bentley, M. J., 1999. Volume of Antarctic ice at the last glacial maximum, and its impact on global sea level change. *Quat. Sci. Rev.*, 18: 1569–1995.

Cazenave, A., Remy, F., Dominh, K. & Douville, H., 2000. Global ocean mass variation, continental hydrology and the mass balance of Antarctica ice sheet at seasonal time scale. *Geophys. Res. Lett.*, 27: 3755–3758.

Cervellati, R. & Geoscience Standing Scientific Group (GSSG), 2003 *[online]*. *Composite Gazetteer of Antarctica*, Scientific Committee on Antarctic Research (SCAR) and Programma Nazionale di Ricerche in Antartide. http://www3.pnra.it/SCAR_GAZE, cited: Feb. 2004, updated: Apr. 2004.

Church, J., 2002. *Changes in Sea Level, IPCC Third Scientific Assessment of Climatic Change*. Cambridge University Press, Cambridge.

Dahlen, F. A. & Tromp, J., 1998. *Theoretical Global Seismology*. Princeton University Press, Princeton.

Danesi, S. & Morelli, A., 2001. Structure of the upper mantle under the Antarctic Plate from surface wave tomography. *Geophys. Res. Lett.*, 28: 4395–4398.

Davis, J. L. & members of BIFROST, 1996. GPS measurements to constrain geodynamic processes in Fennoscandia. *EOS*, 77: 337–341.

Denton, G. H. & Hughes, T. J., 2002. Reconstructing the Antarctic ice sheet at the last glacial maximum. *Quat. Sci. Rev.*, 21: 193–202.

Denton, G. H., Prentice, M. L. & Burckle, L. H., 1991. *Cenozoic History of the Antarctic Ice Sheet*. Oxford University Press, New York.

Dziewonski, A. M. & Anderson, D. L., 1981. Preliminary Reference Earth Model. *Phys. Earth Planet. Inter.*, 25: 297–356.

ESRI, 2003 *[online]*. *Digital Chart of the World (DCW)*, Pennsilvania State University Libraries. http://www.maproom.psu.edu/dcw, cited: Aug. 2003.

Farrell, W. E., 1972. Deformation of the earth by surface loads. *Rev. Geophys.*, 10: 761–797.

Fleming, K., Martinec, Z. & Hagedoorn, J., 2004. Geoid displacement about Greenland resulting from past and present-day mass changes in the Greenland Ice Sheet. *Geophys. Res. Lett.*, 31: L06617, doi:10.1029/2004GL019469.

Gasperini, P., Yuen, D. A. & Sabadini, R., 1990. Effect of lateral viscosity variations on postglacial rebound: implications for recent sea-level trends. *Geophys. Res. Lett.*,

DOI: 10.2312/GFZ.b103-05011

17: 5–8.

Giovinetto, M. B. & Zwally, H. J., 2000. Spatial distribution of net surface accumulation on the Antarctic ice sheet. *Ann. Glaciol.*, 31: 171–176.

Hagedoorn, J. M., 2004. Glaziale Isostasie und rezente Meeresspiegeländerung. *Dissertation*, Universität Stuttgart.

Hagedoorn, J. M., Martinec, Z. & Wolf, D., 2003. A new time-domain method of implementing the sea-level equation in glacial-isostatic adjustment. *Geophys. Res. Abst.*, 5, Session GD10.

Hambrey, M. J. & Hubbard, B., 2004 *[online]*. *The Antarctic ice sheet: Its Initiation and Evolution*, University of Aberystwyth. http://www.aber.ac.uk/ glawww/antarctic.shtml, cited: Feb. 2004.

Han, D. & Wahr, J., 1995. The viscoelastic relaxation of a realistically stratified earth, and a further analysis of postglacial rebound. *Geophys. J. Int.*, 120: 287–311.

Heiskanen, W. A. & Moritz, H., 1967. *Physical Geodesy*. W. H. Freeman, San Francisco.

Huybrechts, P., 1990. The Antarctic ice sheet during the last glacial-interglacial cycle: a three-dimensional experiment. *Ann. Glaciol.*, 14: 115–119.

Huybrechts, P., 2002. Sea-level changes at the LGM from ice-dynamic reconstruction of the Greenland and Antarctic ice sheets during the glacial cycles. *Quat. Sci. Rev.*, 21: 203–231.

International GPS Service, 2003 *[online]*. *Primary ITRF2000 Solution*, Laboratiore de Recherches en Géodésie (LAREG), École National des Science Géographique (ENSG) and Institute Géographique Nationale (IGN). http://lareg.ensg.ign.fr/ITRF/ITRF2000/sol.html, cited: Feb. 2004.

Ivins, E. R., James, T. S., Wu, X., Raymond, C. A. & Yoder, C. F., 2001. Temporal geoid of a rebounding Antarctica and potential measurement by the GRACE and GOCE satellites. In: Sideris, M. G. (ed.), *Gravity, Geoid and Geodynamics 2000*, pp. 361–366. Springer, Heidelberg.

James, T. S. & Ivins, E. R., 1995. Present-day Antarctic ice mass changes and crustal motion. *Geophys. Res. Lett.*, 22: 973–976.

James, T. S. & Ivins, E. R., 1997. Global geodetic signatures of the Antarctic ice sheet. *J. Geophys. Res.*, 102: 605–633.

James, T. S. & Ivins, E. R., 1998. Predictions of Antarctic crustal motions driven by present-day ice sheet evolution and by isostatic memory of the last glacial maximum. *J. Geophys. Res.*, 103: 4993–5017.

Johnston, P., 1993. The effect of spatially non-uniform water loads on predictions of sea-level change. *Geophys. J. Int.*, 114: 615–634.

Kaufmann, G., 2000. Ice-ocean mass balance during the late Pleistocene glacial cycles in view of CHAMP and GRACE satellite missions. *Geophys. J. Int.*, 143: 142–156.

Kaufmann, G., 2002. Predictions of secular geoid changes from Late Pleistocene and Holocene Antarctic ice–ocean mass imbalance. *Geophys. J. Int.*, 148: 340–347.

Klemann, V., 2003. Ebene kompressible viskoelastische Erdmodelle: Anwendung auf glazial-isostatische Deformation der Lithosäre. *Scientific Technical Report STR03/11*, GeoForschungsZentrum Potsdam.

Klemann, V., Wu, P. & Wolf, D., 2003. Compressible viscoelasticity: stability of

DOI: 10.2312/GFZ.b103-05011

solutions for homogeneous plane-earth models. *Geophys. J. Int.*, 153: 569–585.

Křížek, M. & Neittaanmäki, P., 1990. *Finite Element Approximation of Variational Problems and Applications*. J. Wiley, New York.

Lefèvre, F., Lyard, F. H. & Le Provost, C., 2000. FES98: a new global tide finite element solution independent of altimetry. *Geophys. Res. Lett.*, 27: 2717–2720.

Lingle, C. S. & Clark, J. A., 1979. Antarctic ice-sheet volume at 18 000 years b.p. and Holocene sea-level changes at the West Antarctic margin. *J. Glaciol.*, 24: 213–229.

Lythe, M. B., Vaughan, D. G. & BEDMAP Consortium, 2000 *[online]*. *BEDMAP – Bed Topography of the Antarctic, 1:10,000,000 Scale Map*, British Antarctic Survey, Cambridge. http://www.antarctica.ac.uk/aedc/bedmap/, cited: Aug. 2003.

Martinec, Z., 2000. Spectral–finite element approach for three-dimensional viscoelastic relaxation in a spherical earth. *Geophys. J. Int.*, 142: 117–141.

Martinec, Z. & Wolf, D., 1998. Explicit Form of the Propagator Matrix of a Multi-Layered, Incompressible Viscoelastic Sphere. *Scientific Technical Report STR98/08*, GeoForschungsZentrum Potsdam.

Martinec, Z. & Wolf, D., 2004. Inverting the Fennoscandian relaxation-time spectrum in terms of an axisymmetric viscosity distribution with a lithosperic root. *J. Geodyn.*, in press.

Milne, G. A., 1998. Refining models of the glacial isostatic adjustment process. *Ph. D. Thesis*, University of Toronto.

Mitrovica, J. X. & Peltier, W. R., 1989. Pleistocene deglaciation and the global gravity field. *J. Geophys. Res.*, 94: 13651–13671.

Mitrovica, J. X. & Vermeersen, B. L. A. (eds.), 2001. *Ice Sheets, Sea Level and the Dynamic Earth*. American Geophysical Union, Washington.

Nakada, M. & Lambeck, K., 1988. The melting history of the late Pleistocene Antarctic ice sheet. *Nature*, 333: 36–40.

Nakada, M. & Okuno, J., 2003. Perturbations of the earth's rotation and their implications for the present-day mass balance of both polar ice caps. *Geophys. J. Int.*, 152: 124–138.

NASA, 2004 *[online]*. *ICESat*, NASA. http://icesat.gsfc.nasa.gov, cited: Feb. 2004, updated: Sep. 2003.

Peltier, W. R., 1985. The Lageos constraint on deep mantle viscosity: results from a new normal mode method for the inversion of viscoelastic relaxation spectra. *J. Geophys. Res.*, 90: 9411–9421.

Peltier, W. R., 1994. Ice age paleotopography. *Science*, 265: 195–201.

Raymond, C. A., Ivins, E. R., Heflin, M. B., Argus, D. F. & James, T. S., 2000. Tectonic versus isostatic motion in Antarctica. *Geophys. Res. Abst.*, 2, Session G11.

Rignot, E. & Thomas, R. H., 2002. Mass balance of polar ice sheets. *Science*, 297: 1502–1506.

Roe, G. H. & Allen, M. R., 1999. A comparison of competing explanations for the 100,000-yr ice age cycle. *Geophys. Res. Lett.*, 26: 2259–2262.

Scherneck, H. G., Johansson, J. M., Koivula, H., van Dam, T. & Davis, J. L., 2003. Vertical crustal motion observed in the BIFROST project. *J. Geodyn.*, 35: 425–441.

Tamisiea, M. E., Mitrovica, J. X. & Davis, J. L., 2003. A method for detecting rapid

DOI: 10.2312/GFZ.b103-05011

mass flux of small glaciers using local sea level variations. *Earth Planet. Sci. Lett.*, 213: 477–485.

Tregoning, P., Welsh, A., McQueen, H. & Lambeck, K., 2003. The search for post-glacial rebound near the Lambert Glacier, Antarctica. *Earth Planets Space*, 52: 1037–1041.

Tushingham, A. M. & Peltier, W. R., 1991. Ice-3G: a new approach of the late Pleistocene deglaciation based upon geophysical predictions of post-glacial relative sea level change. *J. Geophys. Res.*, 96: 4497–4523.

Varshalovich, D. A., 1989. *Quantum Theory of Angular Momentum*. World Scientific, Singapore.

Vaughan, D. G., Bamber, J. K., Giovinetto, M., Russell, J. & Cooper, P. R., 1999. Reassessment of net surface mass balance in Antarctica. *J. Clim.*, 12: 933–946.

Vaughan, D. G., Marshall, G. J., Connolley, W. M., King, J. C. & Mulvaney, R., 2001. Devil in the detail. *Science*, 293: 1777–1779.

Velicogna, I. & Wahr, J., 2002. A method for seperating Antarctic postglacial rebound and ice mass balance using future ICESat Geoscience Laser Altimeter System, Gravity Recovery and Climate Experiment, and GPS satellite data. *J. Geophys. Res.*, 107: 2263–2273.

Wahr, J. & Velicogna, I., 2003. What might GRACE contribute to studies of post glacial rebound. *Space Sci. Rev.*, 108: 319–330.

Wahr, J., Wingham, D. & Bentley, C., 2000. A method of combining ICESat and GRACE satellite data to constrain Antarctic mass balance. *J. Geophys. Res.*, 105: 16279–16294.

Wieczerkowski, K., Mitrovica, J. X. & Wolf, D., 1999. A revised relaxation-time spectrum for Fennoscandia. *Geophys. J. Int.*, 139: 69–86.

Wolf, D., 1984. The relaxation of spherical and flat Maxwell earth models and effects due to the presence of the lithosphere. *J. Geophys.*, 65: 24–33.

Wolf, D., 1985a. The normal modes of a uniform, compressible Maxwell half-space. *J. Geophys.*, 56: 100–105.

Wolf, D., 1985b. The normal modes of a layered, incompressible Maxwell half-space. *J. Geophys.*, 57: 106–117.

Wolf, D., 1997. *Gravitational Viscoelastodynamics for a Hydrostatic Planet*. Series C, No. 452, Verlag der Bayerischen Akademie der Wissenschaften, München.

Wolf, D., 2003. *Continuum Mechanics in Geophysics and Geodesy: Fundamental Principles*. Schriftenreihe der Institute des Studiengangs Geodäsie und Geoinformatik, Universität Stuttgart, Stuttgart.

Wu, P. & Peltier, W. R., 1982. Viscous gravitational relaxation. *Geophys. J. R. Astr. Soc.*, 70: 435–485.

Zwartz, D., Tregoning, P., Lambeck, K., Johnston, P. & Stone, J., 1999. Estimates of present-day glacial rebound in the Lambert Glacier region, Antarctica. *Geophys. Res. Lett.*, 26: 1461–1464.

DOI: 10.2312/GFZ.b103-05011

List of abbreviations

Earth models

Abbreviation	*Page*	*Description*
LVM	20	low-viscosity model
MP	20	medium-viscosity model
HVM	20	high-viscosity model

Load models

Abbreviation	*Page*	*Description*
VAUG	22	seasonal ice-mass balance based on accumulation data
VUNF	22	seasonal ice-mass balance assuming uniform accumulation
RT02	24	secular ice-mass balance based on mass-balance data for drainage basins
VG02	25	secular ice-mass balance based on accumulation data used for VAUG
ICE-3G-A	28	Pleistocene deglaciation model based on geomorphological data
HUY	29	Pleistocene deglaciation model based on numerical modelling

Satellite-geodetic projects, data bases and organizations

Abbreviation	*Page*	*Description*
ADD	10	Antarctic Digital Database
BIFROST	5	Baseline Inferences for Fennoscandian Rebound Observations, Sea Level and Tectonics
DCW	10	Digital Chart of the World (ESRI product)
ESRI	10	Environmental Systems Research Institute
GFZ	7	GeoForschungsZentrum Potsdam
GPS	7	Global Positioning System
GRACE	7	Gravity Recovery and Climate Experiment (satellite launched 17th March 2002)
ICESat	7	Ice, Cloud, and land Elevation Satellite (satellite launched 12th January 2003)

DOI: 10.2312/GFZ.b103-05011

Abbreviation	*Page*	*Description*
IGS	7	International GPS Service for Geodynamics
InSAR	24	Interferometric Synthetic-Aperture Radar
JPL	7	Jet Propulsion Laboratory
SCAR	7	Scientific Committee on Antarctic Research

Text tokens

Abbreviation	*Page*	*Description*
AIS	5	Antarctic ice sheet
BP	5	before present
ESL	5	equivalent sea level
GIA	5	glacial-isostatic adjustment
LGM	5	last glacial maximum (~ 21 ka BP)
LOD	5	length of day
PGR	5	post-glacial rebound
PREM	18	Preliminary Reference Earth Model
RSL	5	relative sea level
TPW	5	true polar wander

DOI: 10.2312/GFZ.b103-05011

List of symbols

Latin symbols

Symbol	*Page*	*Section*	*Description*
a	59	A.2	radius of the earth
b_{ij}	11	2.1.1	$:= r_{i,j}$
$\bar{C}_{jm}$	58	A.1	fully normalized Stokes coefficient of degree j and order m
d_t	13	2.1.3	first-order material time-derivative operator with respect to t
e			$:= 2.71828...$
e_{G}	58	A.1	geoid height
F_{jm}	58	A.1	spherical-harmonic coefficient of degree j and order m for f
δF_j	58	A.1	degree power of F_{jm}
f^{G}	59	A.2	Green's function
$f_{ij...}$	11	2.1	Lagrangian representation of Cartesian tensor field
$f_{ij...,k}$	11	2.1	gradient of $f_{ij...}$ with respect to X_k
$f^{(0)}_{ij...}$	11	2.1	initial value of $f_{ij...}$
$f^{(\delta)}_{ij...}$	11	2.1	material increment of $f_{ij...}$
$f^{(\Delta)}_{ij...}$	11	2.1	local increment of $f_{ij...}$
$[f_{ij...}]^+_-$	11	2.1.1	interface condition for $f_{ij...}$
G	11	2.1.1	Newton's gravitational constant
g_i	11	2.1.1	gravity force per unit mass
$H(t-t')$	14	2.1.5	Heaviside function
h^{UF}	15	2.3	uniform sea-level change
h^{L}	19	3.2	lithosphere thickness
j	11	2.1.1	Jacobian determinant
m_1	13	2.1.3	bulk-relaxation function
m_2	13	2.1.3	shear-relaxation function
n_i	11	2.1.1	outward unit normal
p	12	2.1.2	mechanical pressure
P	12	2.1.2	number of finite elements
P_{jm}	58	A.1	associated Legendre function of degree j and order m
q^h_j	59	A.2	load Love number of degree j for u_r

DOI: 10.2312/GFZ.b103-05011

Symbol	*Page*	*Section*	*Description*
q_j^k	59	A.2	load Love number of degree j for $\phi^{(\Delta)}$
r_i	11	2.1	current position of particle
$\bar{S}_{jm}$	58	A.1	fully normalized Stokes coefficient of degree j and order m
$s^{\mathrm{I\|O}}$	15	2.3	ice-|ocean-thickness change
$< s^{\mathrm{I}} >$	15	2.3	spatial average of s^{I}
$s^{\mathrm{UF\|NU}}$	15	2.3	uniform|non-uniform part of s^{O}
t	11	2.1	current time epoch
t'	11	2.1.1	excitation time epoch
t_{ij}	11	2.1.1	Cauchy stress
u_i	11	2.1	displacement
u_r	59	A.2	radial surface displacement
u_r^{obs}	53	6.2.1	observed land uplift
X_i	11	2.1	initial position of particle
Y_{jm}	58	A.1	surface spherical-harmonic function of degree j and order m

Greek and calligraphic symbols

Symbol	*Page*	*Section*	*Description*
δ_{ij}	11	2.1.1	Kronecker symbol
ϵ_{ij}	13	2.1.4	linearized strain
$\epsilon_{ij}^{\mathrm{D}}$	13	2.1.4	deviatoric part of ϵ_{ij}
$\mathcal{E}$	14	2.2	energy functional
$\mathcal{F}$	14	2.2	linear functional
η	13	2.1.3	shear viscosity
$\eta^{\mathrm{UM\|LM}}$	19	3.2	upper-|lower-mantle viscosity
ϑ	58	A.1	colatitude
κ	13	2.1.4	elastic bulk modulus
λ	12	2.1.2	composition
$\mathcal{M}_{ij}$	11	2.1.1	anisotropic relaxation functional
μ	14	2.1.5	elastic shear modulus
ξ	12	2.1.2	state function
π			:= 3.14159...
ρ	11	2.1.1	volume-mass density
ρ^{I}	15	2.3	ice volume-mass density (910 kg/m^3)
ρ^{O}	15	2.3	ocean volume-mass density (1020 kg/m^3)

DOI: 10.2312/GFZ.b103-05011

Symbol	*Page*	*Section*	*Description*
σ	11	2.1.1	interface- or surface-mass density
$\sigma^{\mathrm{I\|O}}$	15	2.3	ice|ocean surface-mass density
τ_{ij}	11	2.1.1	Piola-Kirchhoff stress
ϕ	11	2.1.1	gravitational potential
φ	58	A.1	longitude
ψ	12	2.1.2	entropy density
$\mathcal{O}$	15	2.3	ocean function
$\mathbf{\Omega}$	59	A.2	solid angle associated with ϑ and φ

DOI: 10.2312/GFZ.b103-05011

List of figures

DOI: 10.2312/GFZ.b103-05011

List of tables

DOI: 10.2312/GFZ.b103-05011